LETTER

doi:10.1038/nature13585

Inappropriate p53 activation during development induces features of CHARGE syndrome

Jeanine L. Van Nostrand[1], Colleen A. Brady[1]†, Heiyoun Jung[1], Daniel R. Fuentes[2], Margaret M. Kozak[1]†, Thomas M. Johnson[1]†, Chieh-Yu Lin[3], Chien-Jung Lin[4], Donald L. Swiderski[5], Hannes Vogel[3], Jonathan A. Bernstein[6], Tania Attié-Bitach[7,8], Ching-Pin Chang[9], Joanna Wysocka[2,4], Donna M. Martin[10,11] & Laura D. Attardi[1,12]

CHARGE syndrome is a multiple anomaly disorder in which patients present with a variety of phenotypes, including ocular coloboma, heart defects, choanal atresia, retarded growth and development, genitourinary hypoplasia and ear abnormalities[1]. Despite 70–90% of CHARGE syndrome cases resulting from mutations in the gene *CHD7*, which encodes an ATP-dependent chromatin remodeller, the pathways underlying the diverse phenotypes remain poorly understood[2]. Surprisingly, our studies of a knock-in mutant mouse strain that expresses a stabilized and transcriptionally dead variant of the tumour-suppressor protein p53 ($p53^{25,26,53,54}$)[3], along with a wild-type allele of *p53* (also known as *Trp53*), revealed late-gestational embryonic lethality associated with a host of phenotypes that are characteristic of CHARGE syndrome, including coloboma, inner and outer ear malformations, heart outflow tract defects and craniofacial defects. We found that the $p53^{25,26,53,54}$ mutant protein stabilized and hyperactivated wild-type p53, which then inappropriately induced its target genes and triggered cell-cycle arrest or apoptosis during development. Importantly, these phenotypes were only observed with a wild-type *p53* allele, as $p53^{25,26,53,54/-}$ embryos were fully viable. Furthermore, we found that CHD7 can bind to the *p53* promoter, thereby negatively regulating *p53* expression, and that CHD7 loss in mouse neural crest cells or samples from patients with CHARGE syndrome results in p53 activation. Strikingly, we found that *p53* heterozygosity partially rescued the phenotypes in *Chd7*-null mouse embryos, demonstrating that p53 contributes to the phenotypes that result from CHD7 loss. Thus, inappropriate p53 activation during development can promote CHARGE phenotypes, supporting the idea that p53 has a critical role in developmental syndromes and providing important insight into the mechanisms underlying CHARGE syndrome.

Unrestrained p53 activity induced by loss of the negative regulators MDM2 or MDM4 causes early embryonic lethality[4]. To explore the role of transcriptional activation by p53 in promoting developmental failure, we examined embryonic development in knock-in mice carrying mutations in one or both of p53's two transcriptional activation domains ($p53^{25,26}$ and $p53^{25,26,53,54}$; Fig. 1a and Extended Data Fig. 1). These mutations both disrupt the p53–MDM2 interaction—recapitulating loss of MDM2 regulation—and compromise transactivation[3]. Expression of $p53^{25,26}$, whose ability to transactivate most (but not all) p53 target genes is severely impaired, caused early embryonic lethality[5] (at embryonic day (E) 10.5; Extended Data Fig. 2a–c). Surprisingly, $p53^{25,26,53,54/+}$ embryos ($p53^{25,26,53,54}$ is transactivation dead) also exhibited embryonic lethality but between E13.5 and E15.5 (Extended Data Tables 1 and 2). Lethality associated with $p53^{25,26,53,54}$ depended on the presence of a wild-type *p53* allele, as $p53^{25,26,53,54/-}$ adult mice were viable (Extended Data Fig. 2b, d). This observation is in contrast to the embryonic lethality of $p53^{25,26/-}$ mice, which probably results from the residual transactivation potential of $p53^{25,26}$ on genes such as *Bax*[3] (Extended Data Fig. 2a, b). Our findings underscore the importance of transactivation for the embryonic lethality induced by stabilized p53 (because $p53^{25,26,53,54/-}$ mice are viable), as well as revealing an intriguing genetic interaction between $p53^{25,26,53,54}$ (which is transactivation dead) and wild-type p53 during development.

Analysis of $p53^{25,26,53,54/+}$ embryos identified numerous gender-independent developmental phenotypes that were absent in littermate controls (Figs 1 and 2 and Extended Data Figs 3 and 4). E13.5 and older $p53^{25,26,53,54/+}$ embryos commonly displayed exencephaly, as well as craniofacial defects, including square-shaped faces, short lower jaws, cleft lip and cleft palate (Fig. 1b, c and Extended Data Fig. 4a, b). Furthermore, $p53^{25,26,53,54/+}$ embryos displayed defects in external ear formation (Fig. 1d) and a spectrum of inner ear defects, ranging from mild (for example, the posterior semi-circular canal (SCC) was either truncated or fused to the common crus (Fig. 1e)) to highly abnormal (for example, extreme inner ear bone malformation). We also observed retinal coloboma in $p53^{25,26,53,54/+}$ embryos (Fig. 1f, g). As a potential contributor to the craniofacial defects, we examined osteogenesis[6] and found delayed bone formation in $p53^{25,26,53,54/+}$ embryos, suggesting growth retardation (Extended Data Fig. 4c). Notably, this constellation of phenotypes is reminiscent of those in human CHARGE syndrome. In particular, the combined presentation of coloboma and inner ear defects is characteristic of CHARGE syndrome and rarely occurs in other conditions[7].

Given this phenotypic overlap with CHARGE syndrome, we examined whether $p53^{25,26,53,54/+}$ embryos display other CHARGE-associated characteristics[8–10]. The hearts in $p53^{25,26,53,54/+}$ embryos possessed the full complement of cell types (Extended Data Fig. 4d) but displayed outflow tract defects (for example, persistent truncus arteriosus and double outlet right ventricle; Fig. 2a and Extended Data Fig. 4e, f) accompanied by ventricular septation defects (data not shown). The atrioventricular cushions also failed to undergo remodelling, foreshadowing potential heart valve defects (Fig. 2b and Extended Data Fig. 4f). Notably, outflow tract and atrioventricular septation defects are highly overrepresented in patients with CHARGE syndrome compared with individuals with isolated congenital heart disease[11]. Additionally, the kidneys and thymi in $p53^{25,26,53,54/+}$ embryos were smaller than those in controls, and the kidneys displayed branching defects (Fig. 2c and Extended Data Fig. 4g). These phenotypes were in contrast to the liver, which exhibited normal

[1]Department of Radiation Oncology, Division of Radiation and Cancer Biology, Stanford University School of Medicine, Stanford, California 94305, USA. [2]Department of Chemical and Systems Biology, Stanford University School of Medicine, Stanford, California 94305, USA. [3]Department of Pathology, Stanford University School of Medicine, Stanford, California 94305, USA. [4]Department of Developmental Biology, Stanford University School of Medicine, Stanford, California 94305, USA. [5]Department of Otolaryngology, The University of Michigan Medical School, Ann Arbor, Michigan 48109, USA. [6]Department of Pediatrics, Stanford University School of Medicine, Stanford, California 94305, USA. [7]Département de Génétique, Hôpital Necker-Enfants Malades, APHP, 75015 Paris, France. [8]Unite INSERM U1163, Université Paris Descartes-Sorbonne Paris Cité, Institut Imagine, 75015 Paris, France. [9]Krannert Institute of Cardiology, Indiana University School of Medicine, Indianapolis, Indiana 46202, USA. [10]Department of Pediatrics, The University of Michigan Medical School, Ann Arbor, Michigan 48109, USA. [11]Department of Human Genetics, The University of Michigan Medical School, Ann Arbor, Michigan 48109, USA. [12]Department of Genetics, Stanford University School of Medicine, Stanford, California 94305, USA. †Present addresses: Cardiovascular Research Center and Division of Cardiology, Department of Medicine, Massachusetts General Hospital, Harvard Medical School, Charlestown, Massachusetts 02129, USA (C.A.B.); Department of Medicine, University of Central Florida, Orlando, Florida 32827, USA (M.M.K.); Department of Emergency Medicine, Oregon Health and Science University, Portland, Oregon 97239, USA (T.M.J.).

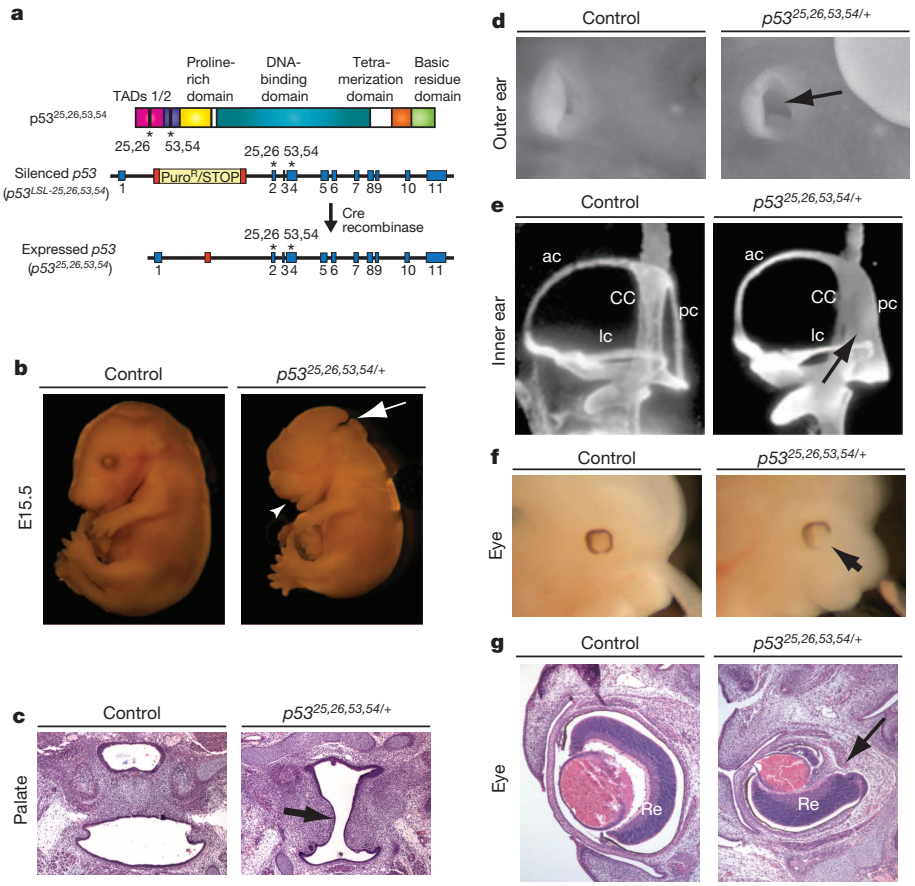

Figure 1 | $p53^{25,26,53,54/+}$ embryos exhibit lethality and diverse craniofacial defects characteristic of CHARGE syndrome. **a**, Top, p53 transcriptional activation domain (TAD) mutant protein with Leu25Gln, Trp26Ser, Phe53Gln, Phe54Ser mutations. Centre and bottom, Cre deletes the *lox–Stop–lox* (LSL) cassette, inducing $p53^{25,26,53,54}$ allele expression. Numbers in *p53* locus schematic indicate exons. Asterisks denote mutations. $Puro^R$, puromycin resistance. **b**, Exencephaly (63%, $n = 35$; arrow) and short lower jaw (74%, $n = 27$; arrowhead) in an E15.5 $p53^{25,26,53,54/+}$ embryo. Original magnification, ×6.3. **c**, Cleft palate (arrow) in an E15.5 $p53^{25,26,53,54/+}$ embryo ($n = 3$). Original magnification, ×100. **d**, Absent external ear pinna (arrow) in an E15.5 $p53^{25,26,53,54/+}$ embryo. (47%, $n = 17$). Original magnification, ×40. **e**, Posterior semi-circular canal (pc) fused to the common crus (CC) (71%, $n = 12$; arrow) in the inner ear of an E13.5 $p53^{25,26,53,54/+}$ embryo. ac, anterior canal; lc, lateral canal. Original magnification, ×20. **f**, Coloboma (arrow) in an E13.5 $p53^{25,26,53,54/+}$ embryo (59%, $n = 17$). Original magnification, ×20. **g**, Retinal coloboma (arrow) in an E15.5 $p53^{25,26,53,54/+}$ embryo. Re, retina. Original magnification, ×100.

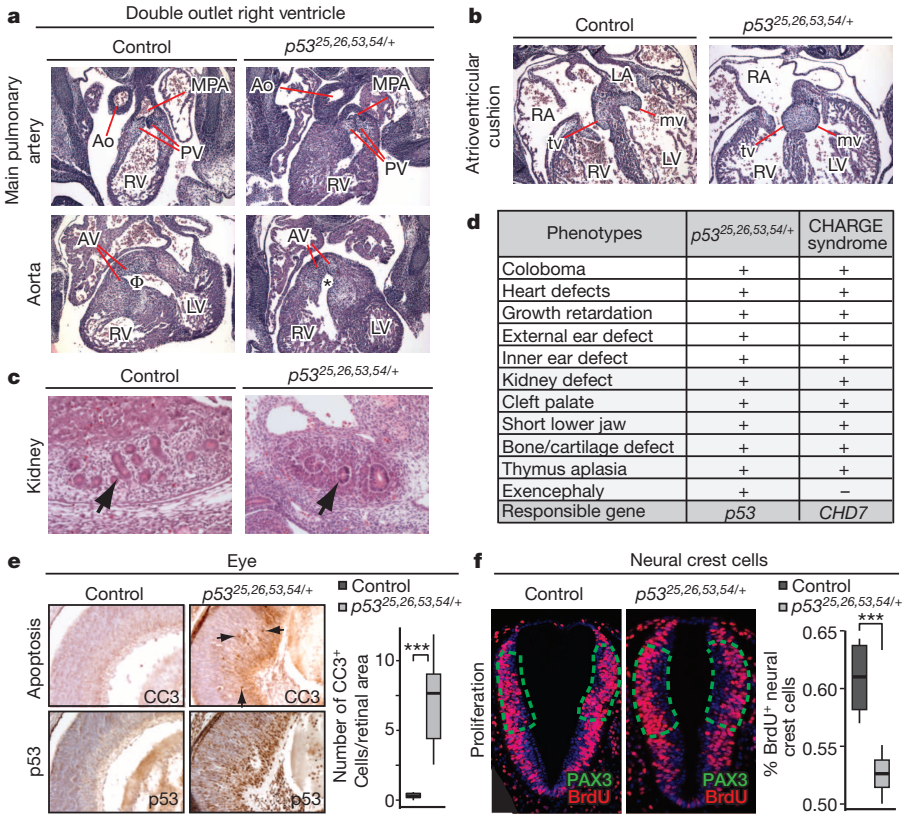

Phenotypes	$p53^{25,26,53,54/+}$	CHARGE syndrome
Coloboma	+	+
Heart defects	+	+
Growth retardation	+	+
External ear defect	+	+
Inner ear defect	+	+
Kidney defect	+	+
Cleft palate	+	+
Short lower jaw	+	+
Bone/cartilage defect	+	+
Thymus aplasia	+	+
Exencephaly	+	–
Responsible gene	*p53*	*CHD7*

Figure 2 | $p53^{25,26,53,54/+}$ embryos exhibit additional features of CHARGE syndrome and p53-dependent cellular responses. **a**, Double outlet right ventricle (DORV) in an E13.5 $p53^{25,26,53,54/+}$ heart (50%, $n = 6$). Top, The main pulmonary artery (MPA) connects via the pulmonary valve (PV) to the right ventricle (RV) in both the control and $p53^{25,26,53,54/+}$ embryos. Bottom, The aorta (Ao) in the control embryo connects to the left ventricle (LV) via the aortic valve (AV) (Φ). The aorta in the $p53^{25,26,53,54/+}$ embryo connects to the RV via the AV (*). Original magnification, ×100. **b**, Abnormal atrioventricular cushions in an E13.5 $p53^{25,26,53,54/+}$ heart (75%, $n = 4$) fail to elongate into mature mitral (mv, arrowhead) and tricuspid (tv, arrow) valves. LA, left atrium; RA, right atrium. Original magnification, ×100. **c**, E13.5 $p53^{25,26,53,54/+}$ kidneys are smaller (79%), with fewer glomeruli (arrow) on average than controls (13 glomeruli on average in controls versus 3 glomeruli on average in mutants; $n = 5$). Original magnification, ×200. **d**, $p53^{25,26,53,54/+}$ embryonic phenotypes observed in CHARGE syndrome (+, present; −, absent). **e**, Left, Cleaved caspase 3 (CC3, top) and p53 (bottom) immunohistochemistry in E15.5 retinas. Arrows denote CC3-positive cells. Right, The number of CC3-positive cells per retinal area is shown. ***, P value = 0.007, one-tailed Welch's t-test ($n = 5$). Original magnification, ×400. **f**, 5-Bromodeoxyuridine (BrdU) immunofluorescence in E9.5 PAX3-positive neural crest cells (NCCs) (delineated by the green dotted line) (see Extended Data Fig. 6c). Right, The percentage of BrdU-positive cells in the total $PAX3^+$ NCC population ***, P value = 0.004, one-tailed Student's t-test ($n = 4$). Original magnification, ×200.

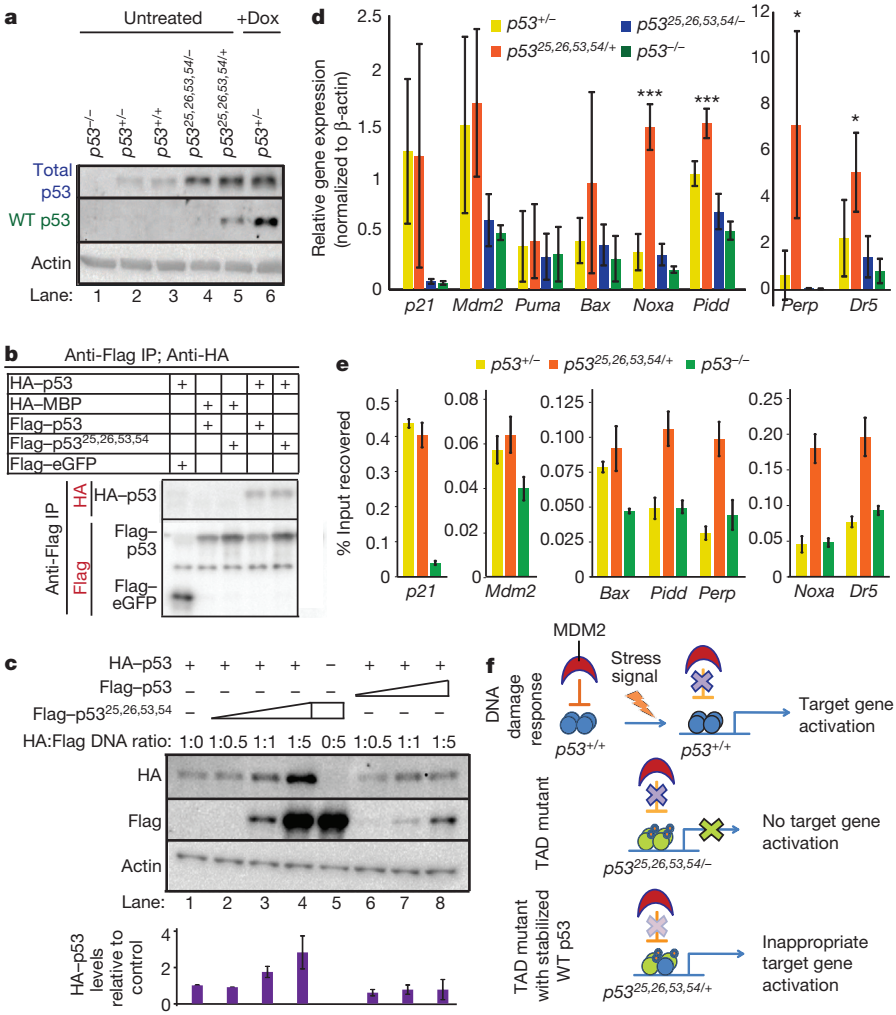

Figure 3 | $p53^{25,26,53,54}$ interacts with and increases wild-type p53 levels and activity. **a**, Immunoblot for total p53 (top row) and wild-type (WT) p53 (second row) in untreated and doxorubicin (Dox)-treated MEFs of the indicated genotypes. β-Actin was used as a loading control. **b**, Anti-Flag immunoprecipitation (IP) and immunoblot of $p53^{-/-}$ MEFs transiently overexpressing HA–p53 and Flag–p53 or Flag–$p53^{25,26,53,54}$. The negative controls were HA–MBP and Flag–enhanced GFP (eGFP). (See also Extended Data Fig. 7b.) **c**, Top, Immunoblot of $p53^{-/-}$ MEFs transiently overexpressing HA–p53 and increasing amounts of Flag–p53 or Flag–$p53^{25,26,53,54}$. Bottom, Mean ± s.d. HA–p53 protein levels relative to lane 1 and normalized to β-actin ($n = 3$). **d**, p53 target gene expression in untreated MEFs of the indicated genotypes, presented as mean ± s.d. normalized to β-actin gene expression ($n = 4$). *, $P < 0.05$; ***, $P < 0.005$, $p53^{25,26,53,54/+}$ versus $p53^{+/-}$ MEFs by two-tailed Student's *t*-test. **e**, Representative analysis from duplicate p53 ChIP analyses of p53 target genes in MEFs of the indicated genotypes relative to input DNA. **f**, Proposed model for how $p53^{25,26,53,54}$ affects p53 activity.

architecture and haematopoiesis (Extended Data Fig. 4h). Evaluation for choanal atresia and external genital defects, which are features of CHARGE syndrome, was precluded by late-gestational embryonic lethality. Importantly, *p53*-null embryos did not display CHARGE-like phenotypes, suggesting that these phenotypes result from p53 activation[12–14] (Extended Data Fig. 5). Collectively, the analysis of $p53^{25,26,53,54/+}$ embryonic phenotypes revealed a strong similarity to phenotypes in patients with CHARGE syndrome (Fig. 2d and Extended Data Fig. 4i), including the presence of hallmarks such as coloboma, ear malformations and heart defects. Additionally, we observed exencephaly and late-gestational lethality, neither of which is commonly reported in CHARGE syndrome. However, it remains possible that fetuses with more severe phenotypes of CHARGE syndrome die *in utero*[15,16].

To understand the underlying cellular basis of the $p53^{25,26,53,54/+}$ embryonic phenotypes, we examined whether p53 induced apoptosis or cell-cycle arrest in these embryos. Analysis of the retina, which is affected in coloboma, and NCCs, which are responsible for some CHARGE phenotypes, revealed more apoptosis and less proliferation in $p53^{25,26,53,54/+}$ embryos than in littermate controls (Fig. 2e, f and Extended Data Fig. 6a, c, d). Similar results were observed in other tissues affected in CHARGE syndrome, including the thymus, neuroepithelium and otic vesicles (Extended Data Fig. 6b, e, f). Thus, both increased apoptosis and reduced proliferation contribute to the $p53^{25,26,53,54/+}$ embryonic phenotypes.

We next investigated the molecular mechanisms by which $p53^{25,26,53,54}$ triggers CHARGE-associated phenotypes. Mutation of p53 residues 25 and 26 inhibits MDM2 interaction, resulting in inappropriate stabilization of the $p53^{25,26,53,54}$ protein, as seen in untreated $p53^{25,26,53,54/+}$ and $p53^{25,26,53,54/-}$ mouse embryonic fibroblasts (MEFs) compared with untreated $p53^{+/-}$ MEFs (Fig. 3a and Extended Data Fig. 7a). Using co-transfection and co-immunoprecipitation, we found that $p53^{25,26,53,54}$ interacts with wild-type p53 (Fig. 3b and Extended Data Fig. 7b). Moreover, overexpressing increasing amounts of Flag–$p53^{25,26,53,54}$ (lanes 2–4), but not Flag–p53 (lanes 6–8), caused haemagglutinin (HA)–p53 protein accumulation (Fig. 3c). Similarly, immunoblot analysis with a wild-type p53-specific antibody revealed that untreated $p53^{25,26,53,54/+}$ MEFs contained more wild-type p53 protein (lane 5) than did untreated $p53^{+/-}$ or $p53^{+/+}$ MEFs (lanes 2 and 3; Fig. 3a). To examine the effects of increased wild-type p53 abundance, we examined p53 target gene expression in $p53^{25,26,53,54/+}$ and control MEFs. $p53^{25,26,53,54}$ alone displayed no transcriptional activity, as seen in genome-wide microarray analyses[3] (Extended Data Fig. 7c) and individual gene quantitative PCR with reverse transcription (qRT–PCR) assays comparing $p53^{25,26,53,54/-}$ and $p53^{-/-}$ MEFs (Fig. 3d). By contrast, $p53^{25,26,53,54}$ combined with wild-type p53 drove elevated expression of certain p53 target genes, including *Noxa* (also known as *Pmaip1*) and *Pidd*, but not *p21* (also known as *Cdkn1a*) and *Mdm2*, relative to the levels in $p53^{+/-}$ and $p53^{+/+}$ MEFs, suggesting that $p53^{25,26,53,54}$ activates wild-type p53 to induce the expression of specific p53 target genes (Fig. 3d and Extended Data Fig. 7d). Similarly, overexpression of $p53^{25,26,53,54}$, but not wild-type p53, in $p53^{+/+}$ MEFs significantly enhanced the expression of certain p53 target genes (Extended Data Fig. 7e). Quantitative chromatin immunoprecipitation (ChIP) analyses revealed that this selective target gene activation resulted from greater binding of p53 to the response elements of particular target genes in $p53^{25,26,53,54/+}$ MEFs than in $p53^{+/-}$ MEFs (Fig. 3e). This pattern probably reflects different affinities of p53-binding sites for p53 such that p53 can only bind to, and activate

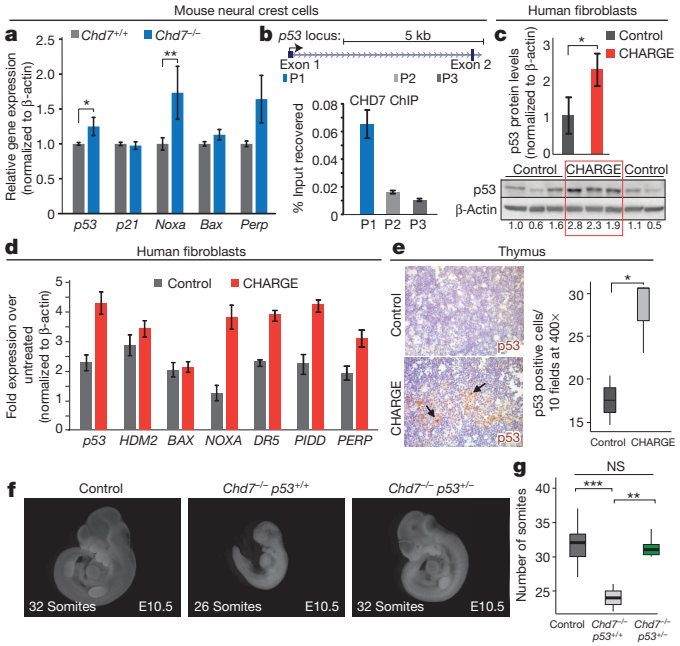

Figure 4 | p53 is activated upon CHD7 deficiency and contributes to *Chd7*-null phenotypes. **a**, p53 target gene expression in $Chd7^{+/+}$ and $Chd7^{-/-}$ (*whi/whi*) NCCs, presented as mean ± s.e.m. normalized to β-actin gene expression ($n = 5$). *, $P < 0.05$; **, $P < 0.01$, one-tailed Mann–Whitney test. **b**, Top, 5′ End of *p53* locus. Bottom, Representative analysis from triplicate ChIP analyses of CHD7 binding to the *p53* promoter (P1) and to negative control open-chromatin regions (P2 and P3), relative to input ± s.d. of technical triplicates. kb, kilobases. **c**, Bottom, p53 immunoblot of human fibroblasts derived from patients with CHARGE syndrome and unaffected individuals (control). The numbers indicate the p53 levels after normalization to β-actin. Top, Data are presented as mean ± s.d. of p53 levels. *, $P = 0.015$, one-tailed Student's *t*-test. **d**, p53 target gene expression in low-serum treated human fibroblasts derived from patients with CHARGE syndrome and unaffected individuals relative to untreated samples. Five CHARGE cell lines were analysed in duplicate. A representative cell line pair is shown, and data are presented as mean ± s.d. of technical triplicates. **e**, Left, p53 immunohistochemistry on thymi from fetuses with CHARGE syndrome and unaffected fetuses. Arrows denote p53-positive cells. Right, The number of p53-positive cells per ten fields at 400× magnification, from one section; $n = 3$. *, $P = 0.037$, one-tailed Student's *t*-test. **f**, Comparison of $Chd7^{-/-}p53^{+/-}$ embryos with control and $Chd7^{-/-}p53^{+/+}$ embryos reveals partial rescue of E10.5 $Chd7^{-/-}p53^{+/-}$ embryos ($Chd7^{-/-}p53^{+/+}$, $n = 3$; $Chd7^{-/-}p53^{+/-}$, $n = 6$). Original magnification, ×20. **g**, Embryo somite number for each genotype. **, $P = 0.0024$; ***, $P = 0.00032$; NS, not significant; two-tailed Student's *t*-test.

transcription from, lower affinity p53-binding sites (such as those in *Noxa* and *Pidd*) when sufficiently stabilized, as is the case in the presence of both $p53^{25,26,53,54}$ and wild-type p53 (ref. 17). Collectively, these findings suggest that in $p53^{25,26,53,54/+}$ embryos, $p53^{25,26,53,54}$ interacts with and stabilizes wild-type p53, probably by compromising the interaction of p53 with MDM2, causing p53 to inappropriately induce target gene expression, cell-cycle arrest and/or apoptosis, and CHARGE-like phenotypes (Fig. 3f).

These observations suggested that p53 may respond to CHD7 deficiency and play a role in CHARGE syndrome. Analysis of *Chd7* expression levels in $p53^{+/-}$ and $p53^{25,26,53,54/+}$ MEFs revealed no significant difference, suggesting that altered *Chd7* levels do not underlie the CHARGE-like phenotypes in $p53^{25,26,53,54/+}$ embryos (Extended Data Fig. 8a). We next assessed whether p53 responds to changes in CHD7 status[15,16,18,19]. Indeed, *p53* and certain p53 target genes were induced in *Chd7*-null NCCs (Fig. 4a and Extended Data Fig. 8b). Interestingly, ChIP analyses showed that CHD7 binds to the *p53* promoter in NCCs, suggesting that CHD7 negatively regulates *p53* expression, providing a mechanism by which CHD7 loss might contribute to a p53 response (Fig. 4b), although not excluding the possibility that CHD7 deficiency could also activate p53 through other mechanisms. To directly assess p53 activation in CHARGE syndrome, we analysed *CHD7*-mutation-positive fibroblasts from patients with CHARGE syndrome and found higher basal p53 protein levels than in controls, as well as p53 target gene induction, following mild stress (Fig. 4c, d). Similarly, analysis of thymi showed more p53-positive thymocytes in *CHD7*-mutation-positive fetuses with CHARGE syndrome than in unaffected fetuses (Fig. 4e). Thus, p53 is activated in *Chd7*-null NCCs and in fibroblasts and tissue from patients with CHARGE syndrome. To establish the role of p53 downstream of *Chd7* loss, we tested whether *Chd7*-null phenotypes are rescued by *p53* heterozygosity. We found that the characteristic *Chd7*-null phenotypes of severe developmental delay and generalized hypoplasia at E10.5 are significantly rescued on a $p53^{+/-}$ background. Specifically, heart development and somite number, an indicator of developmental stage, are rescued, while limb, forebrain and facial morphogenesis are partially rescued (Fig. 4f, g and Extended Data Fig. 8c, d). Thus, *p53* heterozygosity rescues phenotypes caused by CHD7 inactivation, although incompletely, which is consistent with the existence of both p53-dependent and p53-independent responses downstream of CHD7 loss. Collectively, these findings demonstrate that CHD7 deficiency triggers p53 activation and p53-dependent phenotypes.

Our $p53^{25,26,53,54/+}$ mouse strain provides a new model with which to study features that are relevant to CHARGE syndrome. Mouse models of CHARGE syndrome have been generated previously by using *N*-ethyl-*N*-nitrosourea (ENU) mutagenesis or by targeting the *Chd7* locus[20,21]. While $Chd7^{-/-}$ mutants display embryonic lethality at approximately E10.5, $Chd7^{+/-}$ mutants are viable, exhibiting defects of the inner ear, heart, external genitalia and choanae/palate[20,21]. In the inner ear, $Chd7^{+/-}$ mice display truncated lateral SCCs and variably truncated posterior SCCs[20,22], whereas $p53^{25,26,53,54/+}$ embryos primarily exhibit posterior SCC defects or defects in all three SCCs, similarly to patients with CHARGE syndrome, in which all three SCCs are often involved[23]. Interestingly, $Chd7^{+/-}$ mice have not been reported to display the CHARGE hallmarks of coloboma or cardiac outflow tract defects. Thus, the presence of extensive ear defects, heart defects and coloboma in $p53^{25,26,53,54/+}$ embryos highlights the utility of our model for recapitulating a broader form of CHARGE syndrome, potentially representing a phenotype that is intermediate in severity between $Chd7^{+/-}$ and $Chd7^{-/-}$ mutants.

Interestingly, the set of phenotypes of $p53^{25,26,53,54/+}$ embryos is one set in a spectrum of mouse models whereby varying levels of p53 activity trigger different phenotypes. Unlike *Mdm2* deficiency, which results in stabilized, fully active wild-type p53, the combination of wild-type p53 and $p53^{25,26,53,54}$ in $p53^{25,26,53,54/+}$ embryos results in modest p53 activation, causing lethality and phenotypes less severe than *Mdm2* loss[24]. The $p53^{25,26,53,54/+}$ embryonic phenotypes are also in contrast to those seen in other hyperactive p53 mouse models, including one model in which the expression of a carboxy-terminal p53 fragment causes premature ageing and another model in which reduced MDM2 expression triggers lymphopaenia and reduced body weight in adults[25–27]. In these models, the phenotypes manifested without enhanced basal p53 activity or increased p53 stabilization, respectively, potentially explaining the lack of embryonic lethality and the milder phenotypes than observed for $p53^{25,26,53,54/+}$ embryos.

Mechanistically, our observation that p53 activation is sufficient to cause CHARGE-like phenotypes in mice suggested that activated p53 could similarly promote the characteristic defects present in human CHARGE syndrome. Indeed, p53 expression and activity are increased in the presence of CHD7 deficiency, and phenotypes triggered by CHD7 loss are partially rescued by *p53* heterozygosity. This finding is in contrast to a study in which p53 morpholinos failed to rescue Chd7 deficiency in zebrafish, perhaps reflecting species-specific differences[28]. p53 may also function independently of CHD7 to induce the features of CHARGE syndrome, a possibility that is relevant in the ~10–30% of CHARGE cases in which *CHD7* is not mutated. p53 could become

activated in response to other genetic alterations found in CHARGE syndrome, or components of the p53 pathway could themselves be mutated in some CHARGE cases. Our sequencing analysis of the *p53* coding region in 25 *CHD7*-mutation-negative patients with CHARGE failed to reveal any mutations, potentially because modest p53 activation may be difficult to achieve through point mutation, suggesting that mutations in *p53 cis*-regulatory regions or pathway components may be more likely. Significantly, p53 may act as a common node for developmental defects not only in CHARGE syndrome but also in other developmental syndromes, such as 22q11.2 deletion syndrome[29]. Indeed, p53 activation by ribosome dysfunction induces NCC deficiency and craniofacial defects[30]. Future studies will reveal precisely how p53 contributes to CHARGE syndrome and potentially the broader spectrum of human craniofacial and cardiac developmental syndromes.

Online Content Methods, along with any additional Extended Data display items and Source Data, are available in the online version of the paper; references unique to these sections appear only in the online paper.

Received 23 July 2013; accepted 16 June 2014.
Published online 3 August 2014.

1. Davenport, S. L. H., Hefner, M. A. & Mitchell, J. A. The spectrum of clinical features in CHARGE syndrome. *Clin. Genet.* **29,** 298–310 (1986).
2. Jongmans, M. C. J. *et al.* CHARGE syndrome: the phenotypic spectrum of mutations in the *CHD7* gene. *J. Med. Genet.* **43,** 306–314 (2006).
3. Brady, C. A. *et al.* Distinct p53 transcriptional programs dictate acute DNA-damage responses and tumor suppression. *Cell* **145,** 571–583 (2011).
4. Marine, J. C. *et al.* Keeping p53 in check: essential and synergistic functions of Mdm2 and Mdm4. *Cell Death Differ.* **13,** 927–934 (2006).
5. Johnson, T. M., Hammond, E. M., Giaccia, A. & Attardi, L. D. The p53QS transactivation-deficient mutant shows stress-specific apoptotic activity and induces embryonic lethality. *Nature Genet.* **37,** 145–152 (2005).
6. Brock, K. E., Mathiason, M. A., Rooney, B. L. & Williams, M. S. Quantitative analysis of limb anomalies in CHARGE syndrome: correlation with diagnosis and characteristic CHARGE anomalies. *Am. J. Med. Genet. A.* **123A,** 111–121 (2003).
7. Zentner, G. E., Layman, W. S., Martin, D. M. & Scacheri, P. C. Molecular and phenotypic aspects of *CHD7* mutation in CHARGE syndrome. *Am. J. Med. Genet. A.* **152A,** 674–686 (2010).
8. Lalani, S. R. *et al.* Spectrum of *CHD7* mutations in 110 individuals with CHARGE syndrome and genotype–phenotype correlation. *Am. J. Hum. Genet.* **78,** 303–314 (2006).
9. Ragan, D. C., Casale, A. J., Rink, R. C., Cain, M. P. & Weaver, D. D. Genitourinary anomalies in the CHARGE association. *J. Urol.* **161,** 622–625 (1999).
10. Inoue, H. *et al.* Successful cord blood transplantation for a CHARGE syndrome with *CHD7* mutation showing DiGeorge sequence including hypoparathyroidism. *Eur. J. Pediatr.* **169,** 839–844 (2010).
11. Corsten-Janssen, N. *et al.* The cardiac phenotype in patients with a *CHD7* mutation. *Circ. Cardiovasc. Genet.* **6,** 248–254 (2013).
12. Rinon, A. *et al.* p53 coordinates cranial neural crest cell growth and epithelial–mesenchymal transition/delamination processes. *Development* **138,** 1827–1838 (2011).
13. Armstrong, J. F., Kaufman, M. H., Harrison, D. J. & Clarke, A. R. High-frequency developmental abnormalities in p53-deficient mice. *Curr. Biol.* **5,** 931–936 (1995).
14. Lengner, C. J. *et al.* Osteoblast differentiation and skeletal development are regulated by Mdm2–p53 signaling. *J. Cell Biol.* **172,** 909–921 (2006).
15. Sanlaville, D. *et al.* Phenotypic spectrum of CHARGE syndrome in fetuses with *CHD7* truncating mutations correlates with expression during human development. *J. Med. Genet.* **43,** 211–217 (2006).
16. Legendre, M. *et al.* Antenatal spectrum of CHARGE syndrome in 40 fetuses with *CHD7* mutations. *J. Med. Genet.* **49,** 698–707 (2012).
17. Veprintsev, D. B. & Fersht, A. R. Algorithm for prediction of tumour suppressor p53 affinity for binding sites in DNA. *Nucleic Acids Res.* **36,** 1589–1598 (2008).
18. Bajpai, R. *et al.* CHD7 cooperates with PBAF to control multipotent neural crest formation. *Nature* **463,** 958–962 (2010).
19. Schnetz, M. P. *et al.* CHD7 targets active gene enhancer elements to modulate ES cell-specific gene expression. *PLoS Genet.* **6,** e1001023 (2010).
20. Bosman, E. A. *et al.* Multiple mutations in mouse *Chd7* provide models for CHARGE syndrome. *Hum. Mol. Genet.* **14,** 3463–3476 (2005).
21. Hurd, E. *et al.* Loss of *Chd7* function in gene-trapped reporter mice is embryonic lethal and associated with severe defects in multiple developing tissues. *Mamm. Genome* **18,** 94–104 (2007).
22. Adams, M. E. *et al.* Defects in vestibular sensory epithelia and innervation in mice with loss of *Chd7* function: implications for human CHARGE syndrome. *J. Comp. Neurol.* **504,** 519–532 (2007).
23. Morimoto, A. K. *et al.* Absent semicircular canals in CHARGE syndrome: radiologic spectrum of findings. *AJNR Am. J. Neuroradiol.* **27,** 1663–1671 (2006).
24. de Oca Luna, R. M., Wagner, D. S. & Lozano, G. Rescue of early embryonic lethality in *mdm2*-deficient mice by deletion of *p53*. *Nature* **378,** 203–206 (1995).
25. Mendrysa, S. M. *et al. mdm2* is critical for inhibition of p53 during lymphopoiesis and the response to ionizing irradiation. *Mol. Cell. Biol.* **23,** 462–472 (2003).
26. Mendrysa, S. M. *et al.* Tumor suppression and normal aging in mice with constitutively high p53 activity. *Genes Dev.* **20,** 16–21 (2006).
27. Tyner, S. D. *et al.* p53 mutant mice that display early ageing-associated phenotypes. *Nature* **415,** 45–53 (2002).
28. Balow, S. A. *et al.* Knockdown of *fbxl10/kdm2bb* rescues *chd7* morphant phenotype in a zebrafish model of CHARGE syndrome. *Dev. Biol.* **382,** 57–69 (2013).
29. Corsten-Janssen, N. *et al.* More clinical overlap between 22q11.2 deletion syndrome and CHARGE syndrome than often anticipated. *Mol. Syndromol.* **4,** 235–245 (2013).
30. Jones, N. C. *et al.* Prevention of the neurocristopathy Treacher Collins syndrome through inhibition of p53 function. *Nature Med.*14 125–133 (2008).

Supplementary Information is available in the online version of the paper.

Acknowledgements We thank S. Spano-Mello, K. T. Bieging, N. Raj and M. Monje-Deisseroth for reading the manuscript and S. E. Artandi and T. Williams for discussion. We thank H. Chou for immunohistochemistry assistance; E. L. Van Nostrand, P. Lavori, and A. McMillian for statistical analysis; K. Weinberg and D. Min for thymus analysis assistance; M. Shkreli for kidney analysis assistance; B. Liu and J. A. Helms for craniofacial analysis assistance; and M. Bowen for *Chd7* mouse experiment assistance. We thank S. E. Artandi for plasmids; S. E. Artandi and P. Khavari for control human fibroblast cell lines; D. Lane and B. Vojtesek for wild-type p53-specific antibody (pAB242); P. Scacheri for wild-type and *Chd7*-null mouse embryonic stem cells; and T. Denecker and G. Goudefroye for *TP53* sequencing in patients. This work was supported by funding from the NSF and NCI (grant number 1F31CA167917-01) to J.L.V.N.; from the NIH (RO1 GM095555) to J.W.; from the American Heart Association (12EIA8960018), March of Dimes Foundation (#6-FY11-260) and NIH (RO1 HL118087 and RO1 HL121197) to C.-P.C.; from the NIH (R01 DC009410) to D.M.M.; and from the ACS, LLS and NIH (RO1 CA140875) to L.D.A.

Author Contributions J.L.V.N. designed and carried out experiments, interpreted data and wrote the manuscript. C.A.B. generated the *p53*[25,26,53,54] mice, designed and carried out experiments, and interpreted data. H.J. performed p53 ChIP analyses. M.M.K. and T.M.J. performed certain mouse analyses. D.R.F. and J.W. performed NCC differentiation and CHD7 ChIP analyses. C-Y.L., C-J.L. and C-P.C. assisted with heart analyses. D.L.S. and D.M.M. performed inner ear analyses, interpreted data and provided human fibroblasts. H.V. assisted with histological analyses. J.A.B. generated CHARGE and control human fibroblast lines. T.A.-B. performed *TP53* sequencing analysis in patients and supplied CHARGE thymus samples. L.D.A. designed experiments, interpreted data and wrote the manuscript.

Author Information Reprints and permissions information is available at www.nature.com/reprints. The authors declare no competing financial interests. Readers are welcome to comment on the online version of the paper. Correspondence and requests for materials should be addressed to L.D.A. (attardi@stanford.edu).

METHODS

Mouse breeding and analysis. Conditional *p53* mutant mice were described previously[3,5]. $p53^{LSL\text{-}mut/+}$ males were crossed to *CMV-Cre* females, and timed pregnancies were conducted[31]. Genotyping analysis was performed using yolk sac DNA. Males were identified using the PCR for the Y-chromosome-specific *Zfy* gene. As reported[31], we observed mosaic Cre activity in some embryos, reflected by incomplete or no *lox–Stop–lox* deletion in PCR analysis of yolk sacs and in p53 immunohistochemical analysis in embryos. Embryos that showed little to no recombination of the *lox–Stop–lox* allele were kept separate for all analyses. In the text and figure labels, the Cre nomenclature for both control and $p53^{25,26,53,54/+}$ embryos is excluded for simplicity. The genotypes of $p53^{25,26,53,54/+}$ mice carrying a *CMV-Cre* transgene lack the LSL designation because the *lox–Stop–lox* element has been deleted from the genome. Controls in analyses comprise littermate embryos both with and without the *CMV-Cre* transgene (Extended Data Fig. 3). Mice were maintained on a mixed 129/Sv; C57BL/6J background. *Chd7*-deficient gene-trapped mice were described previously[21]. Controls for embryo somite number rescue analysis comprised $Chd7^{+/+}p53^{+/+}$, $Chd7^{+/+}p53^{+/-}$, $Chd7^{+/-}p53^{+/+}$ and $Chd7^{+/-}p53^{+/-}$ embryos. Sample sizes were estimated, based on previous embryogenesis work, to be able to reach significant conclusions. For example, using a chi-squared test, we can estimate that 24 embryos are required to obtain a significance level of 5% if all homozygous embryos were non-viable and from a heterozygous mating where homozygotes should represent 25% of the total based on Mendelian ratio. All animal work was done in accordance with the Stanford University APLAC.

Embryo tissue analysis. Embryos were examined under a dissecting microscope for the presence of a heartbeat and for other abnormalities, in a blinded fashion, before genotyping, and images of either fixed or live embryos were acquired using the dissecting microscope. Whether mice were alive was determined by the presence of a heartbeat. All analyses were performed on embryos of specified ages as determined by the expected stage of tissue and organ development in control embryos. Within age groups, embryos were randomly assigned for the analysis of individual tissues. Heart, inner ear and craniofacial analyses were performed with the assistance of collaborators who were blinded to the genotypes. Histological analysis was performed on haematoxylin and eosin stained paraffin-embedded sagittal, coronal or transverse embryo sections using standard protocols. Consecutive 7-μm sections were evaluated for heart and craniofacial analyses. Whole-mount images for craniofacial analysis were created by staining embryos in 70% ethanol with ethidium bromide and imaging with ultraviolet radiation. Whole-mount cleaved caspase 3 (CC3) staining was performed as described previously[32] with anti-CC3 antibody (Cell Signaling Technology, 9664), and embryos were developed with diaminobenzidine (DAB) (Vector Labs). Immunohistochemistry and immunofluorescence were performed as described with anti-CC3 antibody, anti-5-bromodeoxyuridine (BrdU) antibody (BD Bioscience, 347580), anti-p53 antibody (Vector Labs, CM5), anti-PAX3 antibody (Iowa Developmental Studies Hybridoma Bank) and human anti-p53 antibody (Santa Cruz Biotechnology, Ab1801) on paraformaldehyde-fixed, paraffin-embedded tissue, and slides were developed with either DAB or imaged by immunofluorescence microscopy. For BrdU staining, the embryos were pulsed before dissection for 20 min with 0.1 mg BrdU per g body weight. CC3- and BrdU-positive cells were quantified and normalized to the area, number of sections or total cell number. Bone and cartilage staining were performed as described previously[33], using Alizarin red and Alcian blue to stain bone and cartilage, respectively. Bone lengths were quantified from measurements on photomicrographs acquired at 6.3× magnification. The areas of the kidney and thymus were calculated from measurements on photomicrographs acquired at 200× magnification. Inner ear analysis using the paint-fill assay was performed as described previously[34]; paint-filled ears were imaged in brightfield using a Leica DMRB stereoscope. All individuals with affected ears that could be scored for both ears exhibited a similar severity of the defect in both ears. Additionally, while different types of analysis precluded investigation of all phenotypes in particular embryos, defects commonly occurred in combination: for example, coloboma and inner ear defects occurred together in 57% of $p53^{25,26,53,54/+}$ embryos examined.

qRT–PCR. For qRT–PCR, MEFs were cultured at subconfluency; RNA was isolated by TRIzol extraction and reverse transcribed using M-MLV Reverse Transcriptase (Invitrogen) and random primers; and PCR was performed in triplicate using the SYBR Green system (QIAGEN and Bio-Rad) and mouse-specific primers for each gene (Supplementary Methods Table 1a) in a 7900HT Fast Real-Time PCR machine (Applied Biosystems). The results were computed relative to a standard curve made with cDNA pooled from all samples[3]. Human fibroblasts were cultured at subconfluency in DMEM with 20% serum or 0.1% serum for 24 h before RNA isolation by TRIzol extraction, and qRT–PCR was performed as above using the SYBR Green system and human-specific primers for each gene (Supplementary Methods Table 1b).

Cell culture, western blot analysis and immunoprecipitation. MEFs were derived from E13.5 embryos. For stable overexpressing MEF lines, wild-type and *p53*-null MEFs were transduced with pWZL-based retroviruses expressing Flag–p53, Flag–$p53^{25,26,53,54}$ or empty vector as described previously[5]. Mutant p53 constructs were made via site-directed mutagenesis to bear Leu25Gln, Trp26Ser, Phe53Gln and Phe54Ser mutations, which were found to incapacitate p53's transactivation capability. In summary, a *p53* cDNA, generated from MEF RNA, was amplified and engineered with AscI and PacI restriction enzyme sites using primers against the second amino acid through the stop codon (5′-TTAGGCGCGCCACTGCCATGG AGGAGTC-3′ and 5′-GGCGTTAATTAATCAGTCTGAGTCAGGCCCCAC-3′). The amplified DNA was subcloned into a pBluescript construct with the multiple cloning site replaced with AscI and PacI sites. The *p53* cDNA underwent site-directed mutagenesis (TTATGG to CAATCG and TTTTTT to CAGTCT) to generate the four mutations. The mutated *p53* cDNA was confirmed by sequencing and subcloned into the appropriate expression vectors (pWZL or pcDNA) that contained three copies of either the HA or Flag tag at the amino terminus, as well as AscI and PacI sites instead of the multiple cloning sites. For western blot analysis, cells were left untreated, treated with 0.2 μg ml^{-1} doxorubicin (Dox) for 8 h or transfected using X-tremeGENE HP (Roche) for 24 h with pcDNA constructs (Flag–p53, Flag–$p53^{25,26,53,54}$, HA–p53 or empty vector). Cells were collected and lysed using RIPA buffer. Western blots were probed with anti-p53 (Vector Labs, CM5, 1:500), anti-wild-type p53 (provided by D. Lane and B. Vojtesek, pAB242)[35], anti-Flag (Sigma, F3165, 1:1,000), anti-HA (Sigma, H6908, 1:1,000) and anti-actin (Sigma, A2228, 1:30,000) antibodies. Immunoprecipitation was performed on MEFs transfected with pcDNA constructs (Flag–p53, Flag–$p53^{25,26,53,54}$, HA–p53, Flag–eGFP or HA–MBP) using M2 anti-Flag agarose beads (Sigma, A2220). Dox-treated $p53^{+/-}$ (Fig. 3a, lane 6) and $p53^{25,26,53,54/-}$ (Fig. 3a, lane 4) MEFs controlled for wild-type p53-specific antibody activity and specificity, respectively. Cells were lysed using RIPA buffer; lysates were added to anti-Flag beads to allow the binding of Flag protein; and bound protein was retrieved by the addition of sample buffer and the centrifugation of beads. Ten per cent input was used for western blot analysis. Human fibroblasts were grown in DMEM with 20% serum, and were lysed using RIPA buffer or were incubated in 0.1% serum for 24 h before collection for RNA analysis. Western blots were probed with anti-p53 antibody (Santa Cruz Biotechnology, DO-1). The differentiation of mouse $Chd7^{+/+}$ and $Chd7^{-/-}$ (*whi*/*whi*) embryonic stem cells into NCCs was performed using an adaptation of a previously described protocol[18,19] that has been further characterized[36]. Importantly, loss of CHD7 function does not affect the induction of NCCs, allowing for generation of the cells for this analysis[18]. Validation of NCC phenotype was performed by assessing the gene expression of the NCC markers *Wnt1*, *Snai1* and *Pax3* (Supplementary Methods Table 1a).

ChIP. Analysis of p53 binding was performed on MEFs of different genotypes. For ChIP, 30–40 × 10^7 cells were collected, and immunoprecipitation was conducted using anti-p53 antibody (Vector Labs, CM5), as previously described[37]. In brief, the cells were crosslinked following trypsinization with 1% formaldehyde and quenched with glycine. Chromatin was sheared using a Bioruptor sonicator (Diagenode), then immunoprecipitated with anti-p53–Dynabeads overnight. Immunoprecipitated DNA was washed, reverse-crosslinked and isolated using a PCR clean-up kit (QIAGEN). Immunoprecipitated DNA was analysed using qRT–PCR with binding-site-specific primers (Supplementary Methods Table 2) and normalized to input. Analysis of p53 binding-site affinities was based on previously reported ChIP-sequencing data and a p53 binding-site algorithm[17,37]. Analysis of CHD7 binding was performed using anti-CHD7 antibody on NCC-like cells differentiated from wild-type or *Chd7*-null (*whi*/*whi*) embryonic stem cells using the same protocol as above[18].

Human samples. All human work was conducted under human subject protocols approved by the Stanford Institutional Review Board (IRB), the University of Michigan UM-IRBMED and the Ethical Committee of d'Ile de France II (N° 2009-164). Informed consent was obtained from participants in the study. Human fibroblasts were obtained by skin biopsy under local anaesthesia from CHARGE patients with *CHD7* mutations and unaffected individuals. Thymi were obtained from pregnancies terminated for severe malformations, in accordance with French law, after genetic counselling, between 24 and 37 weeks of gestation. Detailed clinicopathological examination allowed the diagnosis of CHARGE syndrome, which was confirmed by *CHD7* molecular analysis that identified a *de novo* nonsense mutation in each sample. Age-matched control thymi were obtained from fetuses with isolated brain malformations.

TP53 (*p53*) exome sequence was analysed in a group of 25 *CHD7*-mutation-negative patients with features of CHARGE syndrome, who were selected in the cohort based on the availability of parental DNA for segregation analysis, in case a variant was found. All *TP53* coding exons were analysed by direct sequencing of PCR products comprising the ten coding exons and the adjacent intronic junctions of *TP53* isoform 2 (exons 2 to 11, reference sequence NM_001126112.2) and the alternatively spliced exon 10 of isoforms 3 and 4 (reference sequences NM_001126114.2 and NM_001126113.2). This analysis failed to reveal any mutations within the coding

region (that is, no sequence changes apart from already known single nucleotide polymorphisms).

Statistical analysis. The statistical tests used were Student's *t*-test (equal variance), Welch's *t*-test (unequal variance), the Mann–Whitney test (non-parametric test) and the binomial distribution test. Owing to the presence of embryos with little or no recombination of the *lox–Stop–lox* allele, binomial distribution analysis was used to exclude these embryos and to determine the statistical significance for the viability of $p53^{25,26,53,54/+}$ embryos at each embryonic time point. Additional statistical analyses, with the assistance of the Stanford Biostatistics Core, were performed to assess viability over multiple embryonic time points of *CMV-Cre*; $p53^{25,26,53,54/+}$ embryos that had recombined versus those that had not recombined, as scored by PCR analysis (Extended Data Table 2).

The number of dead $p53^{25,26,53,54/+}$ embryos, as a proportion of the total (dead plus alive), was also analysed using logistic regression, with a factor for genotype and a factor for gestational age. Because some of the totals were small, we assessed significance using a permutation test, comparing the observed phenotype (the ratio of dead embryos) to a set of 10,000 random permutations of the phenotype (keeping the number of dead embryos and the total numbers unchanged at each time point and re-fitting the logistic regression). Note that this analysis assumes the effect of clustering within dams is negligible. The *P* value for the permutation test was 0.0234: 234 out of 10,000 random permutations showed a greater frequency of death in absolute value than the frequency of death observed for $p53^{25,26,53,54/+}$ embryos; the *P* value from logistic regression software was $P = 0.0003$. A model allowing a continuous effect of gestational age was also fitted to explore whether the genotype affected the rate of change in the hazard of death: the slopes over time for $p53^{25,26,53,54/+}$ and control embryos were significantly different ($P = 0.0245$), despite the confidence intervals at each individual time point being wide and overlapping.

31. Schwenk, F., Baron, U. & Rajewsky, K. A *cre*-transgenic mouse strain for the ubiquitous deletion of *loxP*-flanked gene segments including deletion in germ cells. *Nucleic Acids Res.* **23,** 5080–5081 (1995).
32. Sato, T. & Bartunkova, S. Analysis of embryonic vascular morphogenesis. *Methods Mol. Biol.* **137,** 223–233 (2000).
33. Ovchinnikov, D. Alcian blue/alizarin red staining of cartilage and bone in mouse. *Cold Spring Harb. Protoc.* http://dx.doi.org/10.1101/pdb.prot5170 (March 2009).
34. Hurd, E. A., Poucher, H. K., Cheng, K., Raphael, Y. & Martin, D. M. The ATP-dependent chromatin remodeling enzyme CHD7 regulates pro-neural gene expression and neurogenesis in the inner ear. *Development* **137,** 3139–3150 (2010).
35. Lane, D. *et al.* Epitope analysis of the murine p53 tumour suppressor protein. *Oncogene* **12,** 2461–2466 (1996).
36. Rada-Iglesias, A. *et al.* Epigenomic annotation of enhancers predicts transcriptional regulators of human neural crest. *Cell Stem Cell* **11,** 633–648 (2012).
37. Kenzelmann Broz, D. *et al.* Global genomic profiling reveals an extensive p53-regulated autophagy program contributing to key p53 responses. *Genes Dev.* **27,** 1016–1031 (2013).

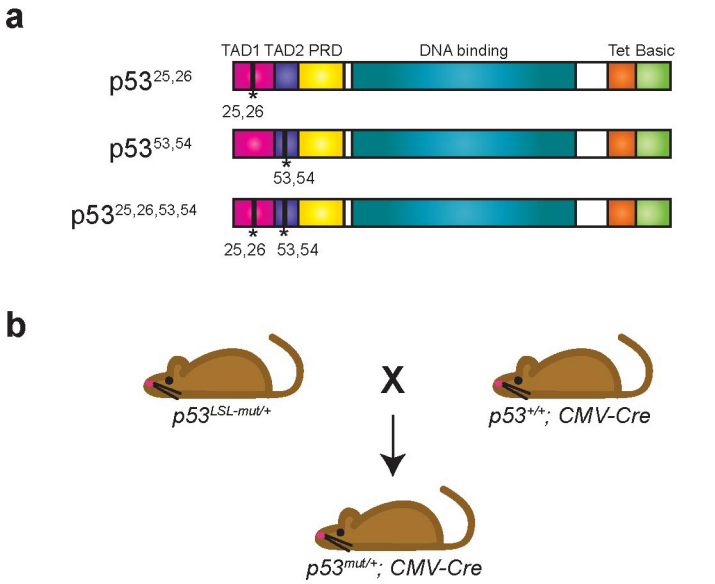

c

Genotype	Functional Genotype
$p53^{+/+}$	Wild-type ($p53^{+/+}$)
$p53^{+/+}$;$CMV\text{-}Cre^{+}$	Wild-type ($p53^{+/+}$)
$p53^{LSL\text{-}25,26,53,54/+}$	$p53^{-/+}$
$p53^{LSL\text{-}25,26,53,54/+}$;$CMV\text{-}Cre^{+}$	$p53^{25,26,53,54/+}$
$p53^{LSL\text{-}25,26,53,54/-}$;$CMV\text{-}Cre^{+}$	$p53^{25,26,53,54/-}$
$p53^{LSL\text{-}25,26,53,54/-}$	$p53^{-/-}$

Extended Data Figure 1 | Model for examining p53-associated developmental phenotypes. **a**, Schematic of $p53^{25,26}$, $p53^{53,54}$ and $p53^{25,26,53,54}$ mutant p53 proteins. Basic, basic-residue-rich domain; PRD, proline-rich domain; TAD, transcriptional activation domain 1 or 2; Tet, tetramerization domain. **b**, $p53^{LSL\text{-}mut/+}$ mice (where *mut* can denote any of the p53 TAD mutants) were crossed to $p53^{+/+}$; *CMV-Cre* mice, which express Cre in the germline, to assess the viability and developmental phenotypes of the *p53*-mutant-expressing progeny. **c**, Table summarizing the actual genotypes and ultimate functional genotypes of progeny from crosses of $p53^{LSL\text{-}25,26,53,54/+}$ and $p53^{+/-}$; *CMV-Cre* mice, as used throughout the manuscript. While $p53^{LSL\text{-}25,26,53,54/+}$; *CMV-Cre* is the actual initial genotype, when Cre acts to delete the *lox–Stop–lox* (LSL) cassette, the genotype is written as $p53^{25,26,53,54/+}$ to reflect this recombination. In the text and figure labels, the Cre nomenclature for both control and $p53^{25,26,53,54/+}$ embryos is excluded for simplicity. Controls for analyses comprised embryos both with and without the *CMV-Cre* transgene, as summarized in Extended Data Fig. 3.

a

$p53^{LSL\text{-}25,26/+}$ x $p53^{+/+}$;CMV-Cre / $p53^{+/-}$;CMV-Cre

Genotype		x $p53^{+/+}$	x $p53^{+/-}$
# Observed Progeny (# Expected Progeny) at E9.5-10.5			
$p53^{+/+}$	Live	8 (8.67)	11 (11.84)
	Dead	0	0
$p53^{+/+}$ Cre^{+}	Live	9 (8.67)	14 (11.84)
	Dead	0	1
$p53^{LSL\text{-}25,26/+}$	Live	9 (8.67)	9 (11.84)
	Dead	0	0
$p53^{25,26/+}$ Cre^{+}	Live	5 (8.67)	8 (11.84)
	Dead	1	2
$p53^{+/-}$	Live	n/a	10 (11.84)
	Dead		0
$p53^{+/-}$ Cre^{+}	Live	n/a	16 (11.84)
	Dead		0
$p53^{LSL\text{-}25,26/-}$	Live	n/a	11 (11.84)
	Dead		0
$p53^{25,26/-}$ Cre^{+}	Live	n/a	8 (11.84)
	Dead		2
		n=32	n=93
		p=0.18	p=0.09

b

$p53^{+/-}$;CMV-Cre X $p53^{LSL\text{-}Mut/+}$

Genotype	$p53^{LSL\text{-}25,26}$	$p53^{LSL\text{-}25,26,53,54}$
# Observed Progeny (# Expected Progeny) at P21		
$p53^{+/+}$	10 (9.625)	15 (13.625)
$p53^{+/+}$ Cre^{+}	17 (9.625)	18 (13.625)
$p53^{LSL\text{-}mut/+}$	15 (9.625)	19 (13.625)
$p53^{mut/+}$ Cre^{+}	0* (9.625)	0** (13.625)
$p53^{+/-}$	18 (9.625)	18 (13.625)
$p53^{+/-}$ Cre^{+}	13 (9.625)	20 (13.625)
$p53^{LSL\text{-}mut/-}$	4 (9.625)	9 (13.625)
$p53^{mut/-}$ Cre^{+}	0* (9.625)	10 (13.625)
	n=77	n=109
	*p=3.42E-05	**p=4.77E-07

c

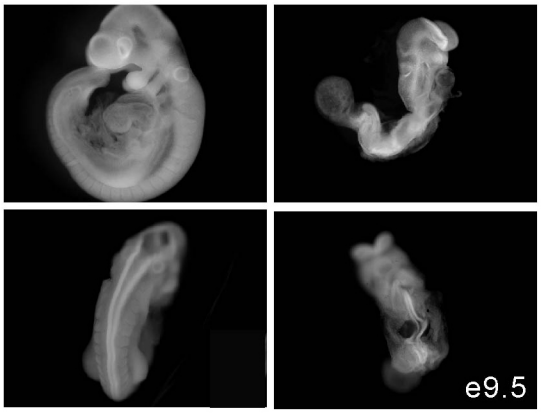

d

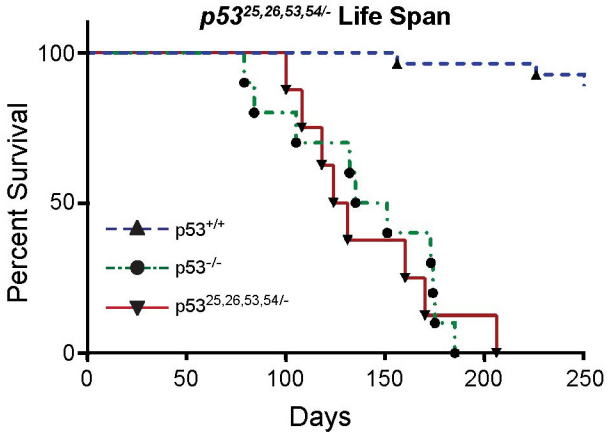

Extended Data Figure 2 | $p53^{25,26,53,54/-}$ mice, but not $p53^{25,26/+}$ or $p53^{25,26/-}$ mice, are viable. **a**, Crosses of $p53^{LSL\text{-}25,26/+}$ with $p53^{+/+}$; *CMV-Cre* or $p53^{+/-}$; *CMV-Cre* mice revealed a decrease in viable pups expressing $p53^{25,26}$ at E9.5–E10.5. The observed numbers of live and dead pups compared with the expected numbers of live pups are indicated: [Observed (Expected)]. The genotypes of the $p53^{25,26/+}$ and $p53^{25,26/-}$ mice carrying a *CMV-Cre* transgene lack the LSL designation because the *lox–Stop–lox* element has been deleted from the genome. Significance was assessed by binomial distribution statistical tests on live pups: $P = 0.18$ for the $p53^{+/+}$ cross and 0.09 for the $p53^{+/-}$ cross. **b**, Crosses of $p53^{LSL\text{-}25,26/+}$ or $p53^{LSL\text{-}25,26,53,54/+}$ with $p53^{+/-}$; *CMV-Cre* mice revealed that $p53^{25,26,53,54/-}$ mice, but not $p53^{25,26/-}$ mice, are viable, as assessed at postnatal day 21 (P21). *mut* denotes either mutant allele. The observed numbers of pups are indicated and compared with the expected numbers of pups: [Observed (Expected)]. The genotypes of $p53^{mut/+}$ and $p53^{mut/-}$ mice carrying a *CMV-Cre* transgene lack the LSL designation because the *lox–Stop–lox* element has been deleted from the genome. The lack of pups is significant at P21 as assessed by binomial distribution statistical tests on live pups compared with expected: $p53^{25,26/+}$ and $p53^{25,26/-}$, * $P = 3.42 \times 10^{-5}$; $p53^{25,26,53,54/+}$, ** $P = 4.77 \times 10^{-7}$. **c**, Whole-mount images of a $p53^{25,26/+}$ embryo (right) at E9.5, displaying developmental delay (top) and neural tube defects, including exencephaly and kinked spine (bottom), compared with a littermate control (left). Original magnification, ×50. **d**, $p53^{25,26,53,54/-}$ mice displayed a shorter lifespan (median lifespan, 128 days; $n = 8$) than wild-type mice (median lifespan, 774 days) and a similar lifespan to $p53^{-/-}$ mice (median lifespan, 143 days), further indicating that the $p53^{25,26,53,54}$ allele itself behaves like a *p53*-null allele; $P < 0.0001$ by Mantel–Cox statistical analysis comparing wild-type and $p53^{25,26,53,54/-}$ mice.

a

Figure	Genotype
Figure 1b	*p53*$^{+/+}$; *CMV-Cre*
Figure 1c	*p53*$^{+/+}$; *CMV-Cre*
Figure 1d	*p53*$^{+/+}$; *CMV-Cre*
Figure 1e	*p53*$^{+/+}$
Figure 1f	*p53*$^{+/-}$; *CMV-Cre*
Figure 1g	*p53*$^{+/+}$; *CMV-Cre*
Figure 2a	*p53*$^{LSL-25,26,53,54/+}$
Figure 2b	*p53*$^{+/+}$
Figure 2c	*p53*$^{+/+}$
Figure 2e	*p53*$^{+/+}$; *CMV-Cre*
Figure 2f	*p53*$^{+/+}$
Figure 4f	*Chd7*$^{+/+}$*p53*$^{+/-}$
Extended Date Figure 2c	*p53*$^{+/+}$
Extended Date Figure 4a	*p53*$^{+/+}$; *CMV-Cre*
Extended Data Figure 4b	*p53*$^{+/+}$; *CMV-Cre*
Extended Data Figure 4c	*p53*$^{+/+}$; *CMV-Cre*
Extended Date Figure 4d	*p53*$^{+/+}$; *CMV-Cre*
Extended Data Figure 4e	*p53*$^{+/+}$
Extended Data Figure 4g	*p53*$^{+/+}$; *CMV-Cre*
Extended Date Figure 4h	*p53*$^{+/-}$; *CMV-Cre*
Extended Date Figure 5a	*p53*$^{+/-}$
Extended Date Figure 5b	*p53*$^{+/-}$
Extended Date Figure 5c	*p53*$^{+/-}$
Extended Date Figure 5d	*p53*$^{+/-}$
Extended Date Figure 5e	*p53*$^{+/+}$
Extended Date Figure 5f	*p53*$^{+/-}$
Extended Date Figure 5g	*p53*$^{+/+}$
Extended Date Figure 5h	*p53*$^{+/-}$
Extended Date Figure 6a	*p53*$^{+/+}$
Extended Data Figure 6b	*p53*$^{LSL-25,26,53,54/+}$
Extended Date Figure 6c	*p53*$^{+/+}$; *CMV-Cre*
Extended Date Figure 6d	*p53*$^{LSL-25,26,53,54/+}$
Extended Date Figure 6e	*p53*$^{+/+}$; *CMV-Cre*
Extended Date Figure 6f	*p53*$^{LSL-25,26,53,54/+}$

b

Phenotype	Male	Female
Coloboma	11	7
Short Jaw	10	10
Outer Ear	3	5
Exencephaly	10	6

Extended Data Figure 3 | Genotypes of the control embryos in the figures and the genders associated with phenotypes. **a**, Table identifying the genotypes of the control embryos shown for each analysis. **b**, Table showing the number of male and female *p53*$^{25,26,53,54/+}$ embryos observed for the indicated phenotypes, as assessed by *Zfy* PCR. The phenotypes are well represented in both sexes.

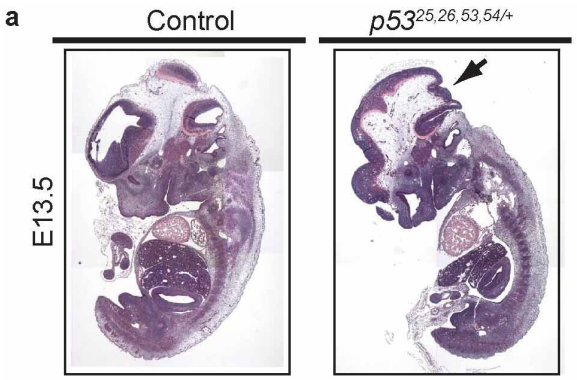

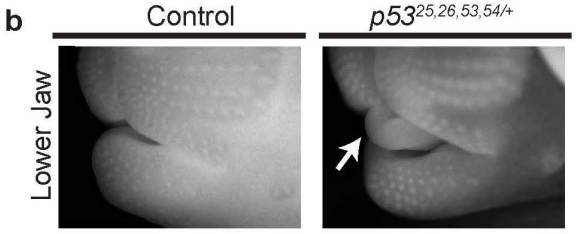

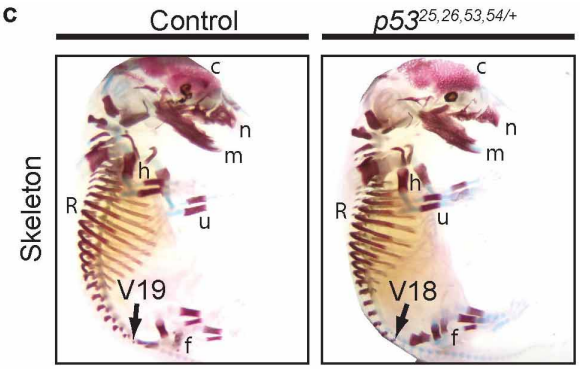

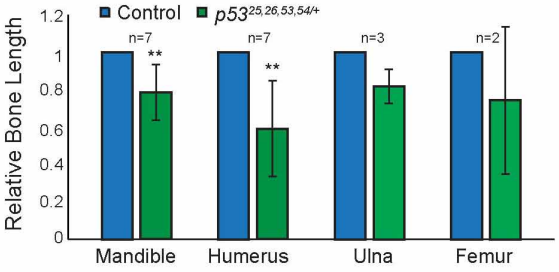

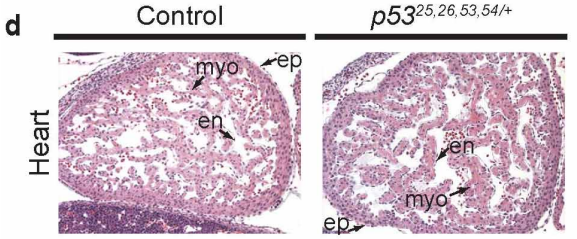

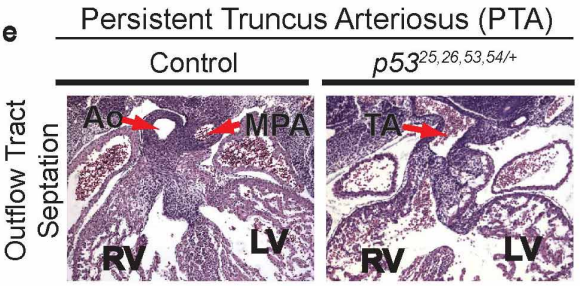

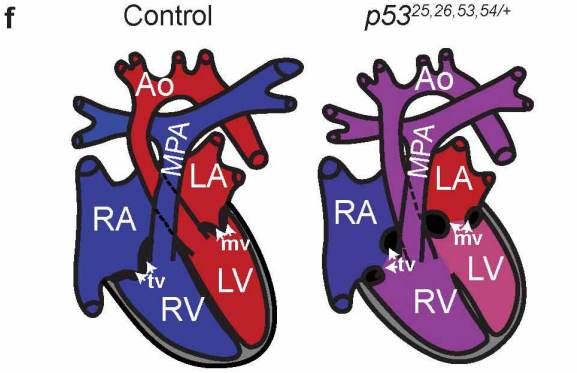

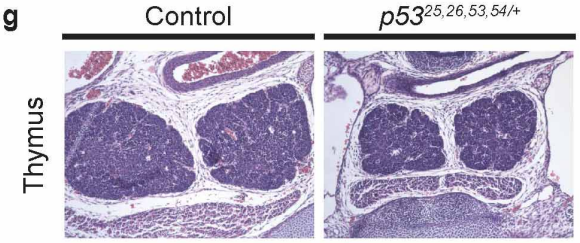

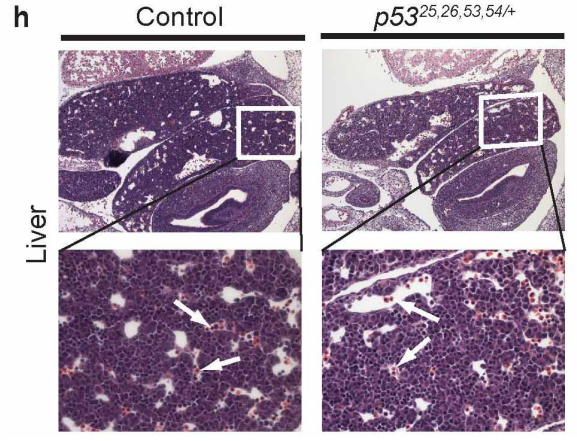

i

Qualitative Phenotypes	p53 25,26,53,54/+	CHARGE Syndrome
Coloboma	59%, n=17	+
Heart Defects - Outflow Tract	83%, n=6	+
Heart Defects - Cushion	75%, n=4	+
External Ear Defect	41%, n=17	+
Inner Ear Defect	71%, n=12	+
Short Lower Jaw	74%, n=27	+
Exencephaly	63%, n=35	-
Responsible Gene	*p53*	*CHD7*

Quantitative Phenotypes	p53 25,26,53,54/+	CHARGE Syndrome
Kidney Defects	79%, n=5	+
Thymus Aplasia	63%, n=4	+
Bone/Cartilage Defects	59-81%, n=7	+
Responsible Gene	*p53*	*CHD7*

Extended Data Figure 4 | $p53^{25,26,53,54/+}$ embryos exhibit additional features of CHARGE syndrome. **a**, Haematoxylin and eosin stained sections of E12.5 control (left) and $p53^{25,26,53,54/+}$ embryos (right). Examination confirmed neural tube closure defects (arrow). Original magnification, ×10. **b**, Close-up image of an ultraviolet-radiation-illuminated, ethidium bromide stained E15.5 $p53^{25,26,53,54/+}$ embryo (right), highlighting the short lower jaw phenotype with protruding tongue (arrow) compared with control littermates (left). Seventy-four per cent of $p53^{25,26,53,54/+}$ embryos ($n = 27$) exhibited a short lower jaw. Cleft lip is not shown. Original magnification, ×40. **c**, Top, Alizarin red (bone) and Alcian blue (cartilage) stained whole mount of an E15.0 $p53^{25,26,53,54/+}$ embryo (right), showing reduced bone density in the cranium (c), nasal cavity (n), shorter ulna (u), humerus (h), mandible (m) and femur (f), as well as reduced bone formation in the ribs (R), where fewer vertebrae are undergoing ossification than in littermate controls (left). The number of vertebrae with bone formation was 19 in the controls (arrow; V19) and 18 in $p53^{25,26,53,54/+}$ embryos (arrow; V18). The severity of the bone and cartilage defects was variable, with the most severe defects evident in embryos with exencephaly and severe craniofacial defects ($n = 7$). Bottom, Quantification of bone lengths shown as percentage of E14.5–15.0 littermate controls. The bone lengths of the mandible, humerus, ulna and femur were measured using the ruler function in Adobe Photoshop on images acquired at 6.3× magnification. Only litters with detectable bone formation in $p53^{25,26,53,54/+}$ embryos were included in bone length analyses: Student's *t*-test; **, $P = 0.008$ (mandible); **, $P = 0.005$ (humerus). **d**, Representative images of haematoxylin and eosin stained sagittal sections of E12.5 control hearts (left) and $p53^{25,26,53,54/+}$ hearts (right), showing all three cardiac cell types in both genotypes. en, endocardium; ep, epicardium; myo, myocardium (arrows). Original magnification, ×200. **e**, A haematoxylin and eosin stained E12.5 $p53^{25,26,53,54/+}$ heart exhibiting persistent truncus arteriosus (PTA) (33%, $n = 6$). The cardiac outflow tract in the control embryo (left) is septated into the aorta (Ao) and main pulmonary artery (MPA), whereas the cardiac outflow tract (truncus arteriosus (TA)) in the $p53^{25,26,53,54/+}$ embryo (right) remains unseptated, resulting in PTA. Original magnification, ×100. **f**, Illustration of a control heart (left) and a $p53^{25,26,53,54/+}$ embryo heart (right), highlighting double outlet right ventricle (DORV) and atrioventricular cushion defects. Both the aorta (Ao) and the MPA flow out of the right ventricle (RV), resulting in mixed oxygenated and deoxygenated blood in the systemic circulation when combined with concurrent ventricular septal defects (VSDs). The atrioventricular cushions remain bulbous and fail to elongate into mature valve leaflets. Red denotes oxygenated blood; blue denotes deoxygenated blood; and purple (pink) denotes mixed oxygenated and deoxygenated blood. mv, mitral valve; tv, tricuspid valve. Original magnification, ×100. **g**, Representative haematoxylin and eosin stained transverse section of thymus from a $p53^{25,26,53,54/+}$ E15.5 embryo (right) reveals a smaller thymus than in littermate controls (left) (63% of controls; $n = 4$). Original magnification, ×200. **h**, Representative haematoxylin and eosin analysis of liver sections from E12.5 controls (left) and $p53^{25,26,53,54/+}$ embryos (right), showing normal liver architecture in both genotypes (top). High magnification image (bottom) of the region of the liver that is outlined by the white box in the top panel shows the presence of nucleated erythrocytes (arrows), indicating proper haematopoiesis. Original magnification top, ×100; bottom, ×400. **i**, Top, Table summarizing the incidence (%) and sample size (*n*) of phenotypes assessed qualitatively in $p53^{25,26,53,54/+}$ embryos. The occurrence of these phenotypes in CHARGE syndrome is also indicated (+, present; −, absent). Bottom, Table summarizing the phenotypes assessed quantitatively in $p53^{25,26,53,54/+}$ embryos relative to controls, shown as the percentage average size of the control (%), with sample size (*n*) also indicated. The occurrence of these phenotypes in CHARGE syndrome is also shown (+, present). A detailed description of the bone and cartilage defects is provided in **c**.

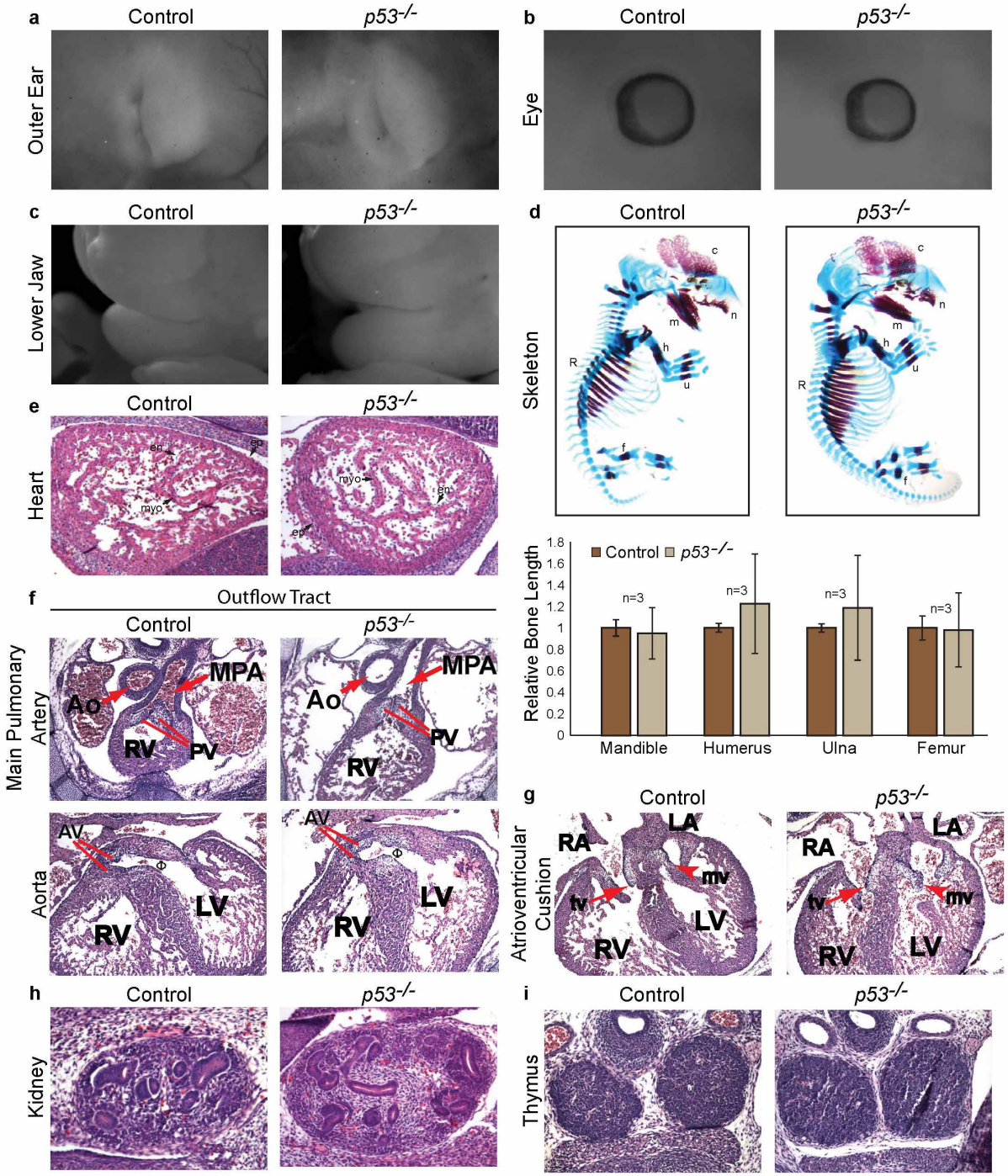

Extended Data Figure 5 | *p53*$^{-/-}$ embryos do not exhibit characteristics of CHARGE syndrome. **a**, Whole-mount image of the external ear of an E15.5 *p53*$^{-/-}$ embryo (right) and a control embryo (left), showing normal ear pinna development. Original magnification, ×100. **b**, Whole-mount image of an E13.5 *p53*$^{-/-}$ embryo (right) and a control embryo (left), showing normal retinal development and no evidence of coloboma. Original magnification, ×100. **c**, Whole-mount image of an E15.5 *p53*$^{-/-}$embryo (right) and a control embryo (left), showing normal lower jaw development. Original magnification, ×40. **d**, Top, Alizarin red (bone) and Alcian blue (cartilage) stained whole-mount E14.5 *p53*$^{-/-}$embryo (right), showing normal long bone formation of the ulna (u), humerus (h), mandible (m), and femur (f) relative to littermate controls (left). Bottom, Quantification of the bone lengths shown as a percentage of E14.5 littermate controls ($n = 3$). Original magnification, ×6.3. **e**, Representative images of haematoxylin and eosin stained sagittal sections of E13.5 control hearts (left) and *p53*$^{-/-}$ hearts (right), showing all three cardiac cell types in both genotypes. en, endocardium; ep, epicardium; myo, myocardium (arrows). Original magnification, ×200. **f**, Analysis of haematoxylin and eosin stained transverse sections of E13.5 *p53*$^{-/-}$ and control hearts revealing normal outflow tract development. Top, The MPA and Ao are fully septated, and the MPA connects to the right ventricle (RV) in *p53*$^{-/-}$ hearts. Bottom, The Ao connects to the left ventricle (LV). The symbol Φ denotes that the ventricular outflow tract connects the LV and AO. AV, aortic valve; PV, pulmonary valve. Original magnification, ×100. **g**, Analysis of transverse sections of haematoxylin and eosin stained E13.5 *p53*$^{-/-}$ hearts (right) reveals normal atrioventricular cushions, which have undergone remodelling to form mature, elongated mitral valves (mv; arrowhead) and tricuspid valves (tv; arrow) similar to in control hearts (left). LA, left atrium; RA, right atrium. Original magnification, ×100. **h**, Haematoxylin and eosin stained sagittal section of kidney from *p53*$^{-/-}$ (right) and control (left) embryos, showing normal renal size and development. Original magnification, ×200. **i**, Haematoxylin and eosin stained transverse section of thymus in a *p53*$^{-/-}$ E13.5 embryo (right) reveals a similar thymus size to that in a littermate control (left). Original magnification, ×200.

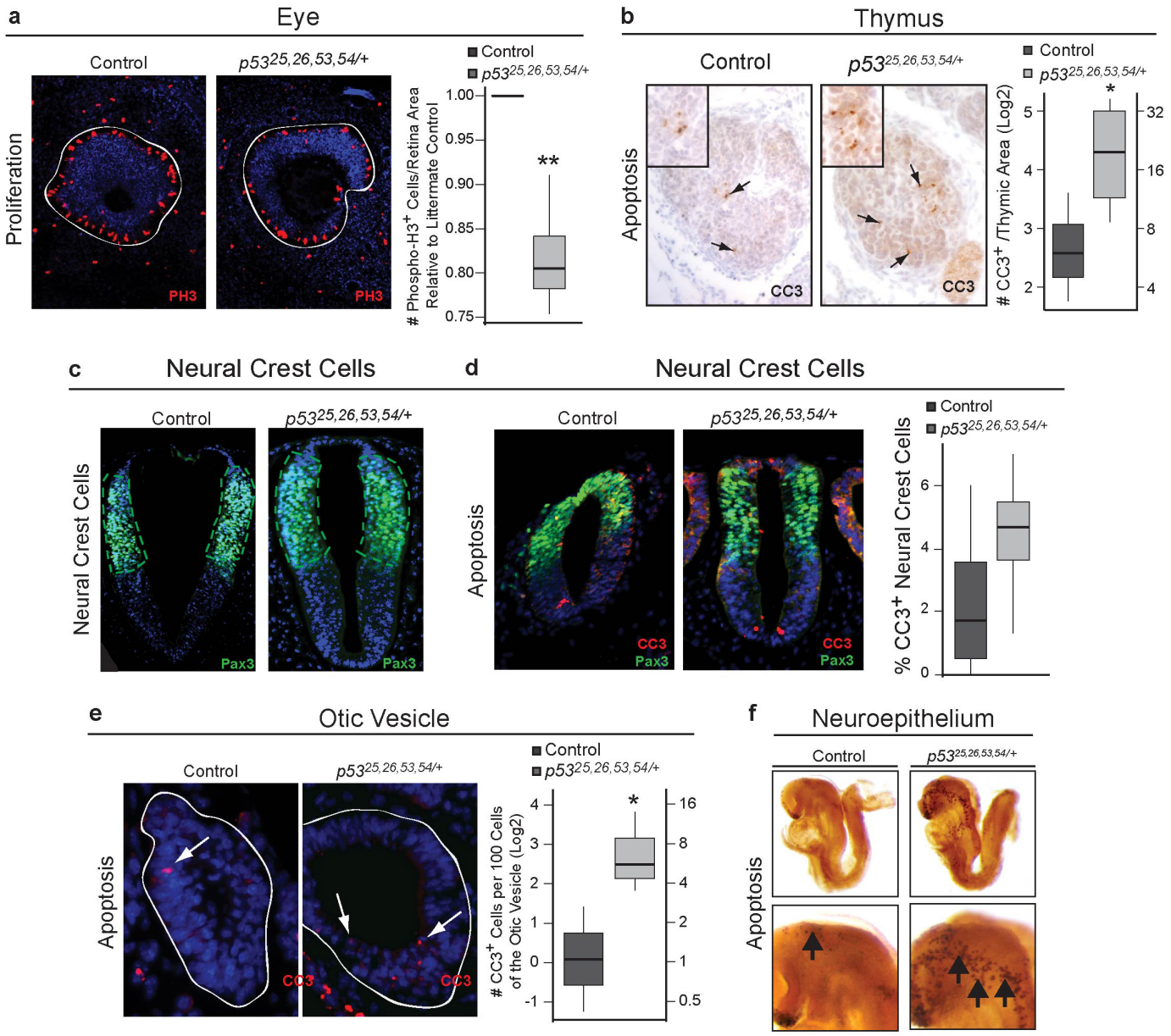

Extended Data Figure 6 | $p53^{25,26,53,54/+}$ embryo tissues display increased apoptosis and decreased proliferation. **a**, Left, Immunofluorescence for phospho-histone H3 (red) in the retina of E13.5 control and $p53^{25,26,53,54/+}$ embryos. Right, Quantification of phospho-H3-positive cells per retina area relative to littermate controls. **, $P = 0.006$ by one-tailed Welch's *t*-test ($n = 4$). Original magnification, ×200. **b**, Left, Immunohistochemistry for cleaved caspase 3 (CC3) in thymi of control (left) and $p53^{25,26,53,54/+}$ (right) embryos. Inset, Magnified image of CC3-positive region. Right, Quantification of CC3-positive cells per thymic area. *, $P = 0.02$ by one-tailed Student's *t*-test ($n = 4$). Original magnification, ×400. **c**, Immunofluorescence for PAX3 (green) in NCCs of E9.5 control and $p53^{25,26,53,54/+}$ embryos was used to identify NCCs in Fig. 2f. Original magnification, ×200. **d**, Left, Immunofluorescence for CC3 (red) and PAX3 (green) in NCCs of E9.5 control and $p53^{25,26,53,54/+}$ embryos. $p53^{25,26,53,54/+}$ embryos have more apoptotic (red) NCCs, as determined by PAX3-positive staining (green), than littermate controls. Right, Quantification of CC3-positive cells per total NCC number. $P = 0.14$ by one-tailed Student's *t*-test ($n = 4$). Original magnification, ×200. **e**, Left, Immunofluorescence for CC3 (red) in the otic vesicles of E9.5 control and $p53^{25,26,53,54/+}$ embryos. Right, Quantification of CC3-positive cells per total cell number. *, $P = 0.03$ by one-tailed Student's *t*-test ($n = 3$). Original magnification, ×200. **f**, CC3 staining in whole-mount E8.5 control and $p53^{25,26,53,54/+}$ embryos reveals enhanced apoptosis in the neuroepithelium of $p53^{25,26,53,54/+}$ embryos (right) but not in controls (left). The close-up shows a magnification of the caudal neuroepithelium (bottom). Arrows indicate CC3-positive regions. Original magnification top, ×50.

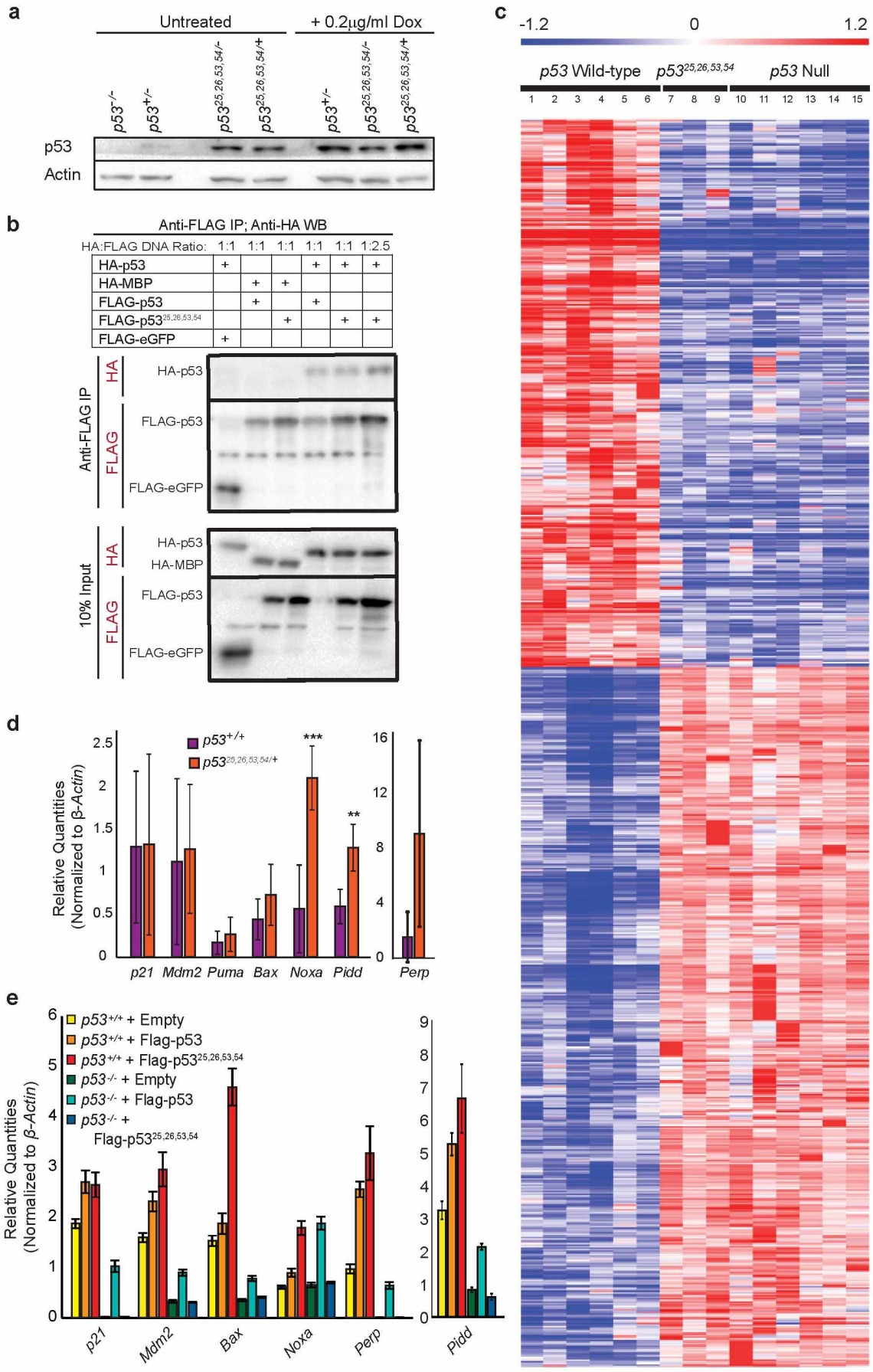

Extended Data Figure 7 | $p53^{25,26,53,54}$ is transactivation dead but augments wild-type p53 activity. **a**, Western blot analysis of p53 protein levels in untreated or doxorubicin-treated (0.2 μg ml^{-1} Dox) $p53^{-/-}$, $p53^{+/-}$, $p53^{25,26,53,54/-}$ and $p53^{25,26,53,54/+}$ MEFs. β-Actin served as a loading control. **b**, Western blot analysis of anti-Flag immunoprecipitation from $p53^{-/-}$ MEFs transiently overexpressing HA–p53 and Flag–p53 or Flag–$p53^{25,26,53,54}$. HA–MBP and Flag–eGFP were used as negative controls. Immunoprecipitated protein and 10% input were probed with either anti-HA or anti-Flag antibodies. (The microgram ratio of HA–p53 to Flag–p53 or Flag–$p53^{25,26,53,54}$ plasmid DNA was 1:1 or 1:2.5, as indicated above the blot (see Fig. 3b). **c**, Heat map examining the transactivation capacity of $p53^{25,26,53,54}$ on p53-dependent genes identified by microarray analysis through comparison of six *HrasV12;* WT *p53* MEF lines with six *HrasV12; p53*-null MEF lines, as previously described[3]. Three independent *HrasV12;* $p53^{25,26,53,54/25,26,53,54}$ MEF lines were analysed, and the gene expression profiles were indistinguishable from those of *HrasV12; p53*-null cells. The numbered columns indicate independent MEF lines. Blue denotes repressed genes, and red denotes induced genes. **d**, qRT–PCR analysis of p53 target gene expression in untreated MEFs derived from $p53^{+/+}$ and $p53^{25,26,53,54/+}$ E13.5 embryos. Graphs indicate the mean ± s.d. from four independent MEF lines after normalization to β-actin gene expression. **, $P < 0.01$; ***, $P < 0.005$; Student's *t*-test. **e**, qRT–PCR analysis of p53 target gene expression in $p53^{+/+}$ and $p53^{-/-}$ MEFs stably transduced with empty vector, Flag–p53 or Flag–$p53^{25,26,53,54}$. The representative gene expression from one experiment is shown: mean ± s.d. of technical triplicates after normalization to β-actin gene expression. The experiment was performed in duplicate.

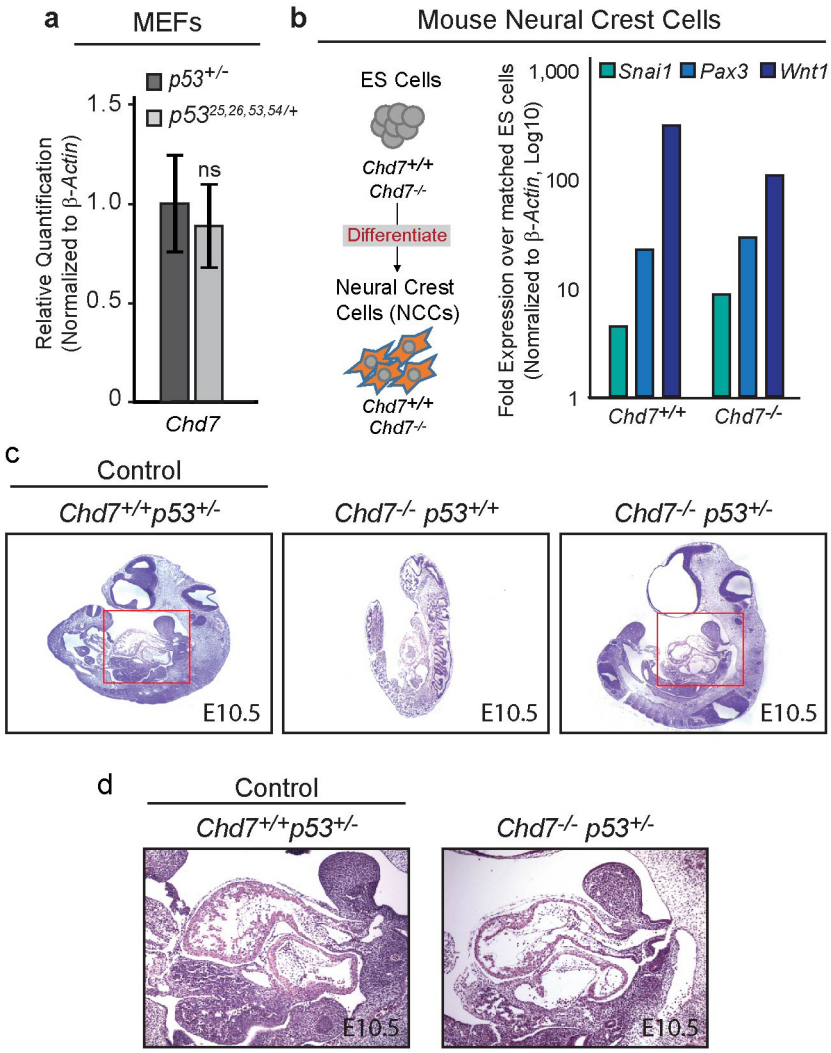

Extended Data Figure 8 | p53 heterozygosity partially rescues *Chd7*-null embryos. **a**, qRT–PCR analysis of *Chd7* expression in untreated MEFs derived from E13.5 $p53^{+/-}$ and $p53^{25,26,53,54/+}$ embryos. The graphs indicate the mean ± s.d. from four independent MEF lines after normalization to β-actin gene expression. ns, not significant. **b**, Left, Schematic of NCC differentiation. Right, Representative qRT–PCR analysis of NCC markers in NCC-like cells differentiated from $Chd7^{+/+}$ and $Chd7^{-/-}$ (*whi*/*whi*) mouse embryonic stem cells normalized to β-actin gene expression and relative to matched embryonic stem cells. **c**, Haematoxylin and eosin stained E10.5 $Chd7^{+/+}p53^{+/-}$ (control), $Chd7^{-/-}p53^{+/+}$ and $Chd7^{-/-}p53^{+/-}$ embryos. The $Chd7^{-/-}p53^{+/+}$ embryo shown is necrotic, as evidenced by cellular autolysis. Original magnification, ×32. **d**, Close-up image of heart region denoted by red box in panel **c**, in E10.5 $Chd7^{+/+}p53^{+/-}$ (control) and $Chd7^{-/-}p53^{+/-}$ embryos. Original magnification, ×100.

Extended Data Table 1 | *p53*$^{25,26,53,54/+}$ mice do not survive to weaning

	p53$^{+/+}$;*CMV-Cre* X *p53*$^{LSL-X/+}$		
Genotype:	***p53***$^{LSL-wt}$	***p53***$^{LSL-53,54}$	***p53***$^{LSL-25,26,53,54}$
	# Observed Progeny (# Expected Progeny) at P21		
p53$^{+/+}$	18 (15)	10 (12)	19 (41.75)
p53$^{+/+}$ *Cre*$^{+}$	21 (15)	14 (12)	68 (41.75)
p53$^{LSL-X/+}$	11 (15)	9 (12)	50 (41.75)
p53$^{X/+}$ *Cre*$^{+}$	10 (15)	15 (12)	0* (41.75)
	n=60 p=0.086	n=48 p=0.876	n=167 *p=7.65E-18

Crosses of *p53*$^{LSL\text{-}wt/+}$, *p53*$^{LSL\text{-}53,54/+}$ or *p53*$^{LSL\text{-}25,26,53,54/+}$ with *p53*$^{+/+}$; *CMV-Cre* mice yield the expected numbers of *p53*$^{wt/+}$ and *p53*$^{53,54/+}$ pups but not *p53*$^{25,26,53,54/+}$ pups at postnatal day 21 (P21). *X* denotes wild-type or mutant allele. The observed numbers of live and dead pups compared with the expected numbers of live pups are indicated: [Observed (Expected)]. p53^{53,54} mutations in the second TAD did not perturb the transcriptional activity of p53 at the genome-wide level and provide a control for the mutation of only these residues. The presence of viable *p53*$^{wt/+}$ and *p53*$^{53,54/+}$ pups suggests that re-expression of p53 in early development using this system does not cause developmental defects. The binomial distribution statistical test shows that the absence of *p53*$^{25,26,53,54/+}$ pups at P21 is significant. *, $P = 7.65 \times 10^{-18}$.

Extended Data Table 2 | $p53^{25,26,53,54/+}$ embryo survival and incidence of exencephaly in live embryos

***p53*$^{+/+}$*;CMV-Cre* X *p53*$^{LSL\text{-}25,26,53,54/+}$**

Genotype:		Embryonic Age: E12.5	E13.5	E14.5	E15.5	E18.5
		# Observed Progeny (# Expected Progeny)				
$p53^{+/+}$	Live	32 (28)	37 (45)	21 (20)	15 (19)	12 (14)
	Dead	*1*	*3*	*2*	*0*	*0*
	Exencephaly	0	0	0	0	0
$p53^{+/+}$ Cre^{+}	Live	27 (28)	59 (45)	20 (20)	17 (19)	20 (14)
	Dead	*4*	*12*	*3*	*1*	*5*
	Exencephaly	0	0	0	1	0
$p53^{LSL\text{-}25,26,53,54/+}$	Live	26 (28)	38 (45)	18 (20)	24 (19)	9 (14)
	Dead	*3*	*3*	*1*	*0*	*0*
	Exencephaly	0	0	0	0	0
$p53^{25,26,53,54/+}$ Cre^{+}	Live	16 (19)	23* (37)	7 (14)	1** (16)	2* (7)
	Dead	*3*	*8*	*11*	*6*	*9*
	Exencephaly	14	8	2	1	1
$p53^{LSL\text{-}25,26,53,54/+}$ Cre^{+} No or incomplete recombination	Live	9	8	6	3	7
	Dead	*1*	*1*	*1*	*0*	*1*
	Exencephaly	0	2	0	0	0
		n=122 p=0.290	n=192 *p=0.019	n=90 p=0.053	n=67 **p=1.24E-05	n=65 *p=0.047

Survival of embryos at E12.5, E13.5, E14.5, E15.5 and E18.5 from timed matings between $p53^{LSL\text{-}25,26,53,54/+}$ and $p53^{+/+}$; *CMV-Cre* mice. The numbers of live mice of each genotype were identified by the presence of a heartbeat. The observed numbers of live and dead pups compared with the expected numbers of live pups are indicated: [Observed (Expected)]. For the $p53^{25,26,53,54/+}$; *Cre* genotype, the number of expected live pups was fewer than for the other genotypes owing to some incidence of incomplete recombination of the LSL element, as detailed below. The number of live embryos exhibiting exencephaly observed at the time of dissection is also indicated (63% over all time points). Females and males, as determined by *Zfy* PCR, exhibited exencephaly with the same frequency. The genotypes of $p53^{25,26,53,54/+}$ embryos carrying a *CMV-Cre* transgene lack the LSL designation because the *lox–Stop–lox* element has been deleted from the genome. As reported[31], we observed mosaic Cre activity in some embryos, reflected by incomplete or no *lox–Stop–lox* deletion in PCR analysis of yolk sac DNA. Embryos that showed little to no recombination of the *lox–Stop–lox* allele were excluded from analyses. Statistical significance for the viability of embryos was assessed using binomial distribution analysis to account for embryos with little or no recombination of the *lox–Stop–lox* allele. The binomial distribution statistical test showed that the absence of live $p53^{25,26,53,54/+}$ embryos at late-gestational time points is significant. E12.5, $P = 0.290$; E13.5, *, $P = 0.019$; E14.5, $P = 0.053$; E15.5, **, $P = 1.24 \times 10^{-5}$; E18.5, *, $P = 0.047$. Logistic regression to compare the viability of *CMV-Cre;* $p53^{25,26,53,54/+}$ embryos with and without complete recombination showed that the increased death of recombined *CMV-Cre;* $p53^{25,26,53,54/+}$ embryos is significant: $P < 0.0001$.